

Energy Dissipation in Synchronous Binary Asteroids

Alex J. Meyer^{a,*}, Daniel J. Scheeres^a, Harrison F Agrusa^b, Guillaume Noiset^c, Jay McMahon^a, Özgür Karatekin^c, Masatoshi Hirabayashi^{d,e} and Ryota Nakano^d

^a*Smead Department of Aerospace Engineering, University of Colorado, Boulder, CO 80303, USA*

^b*Department of Astronomy, University of Maryland, College Park, MD 20742, USA*

^c*Royal Observatory of Belgium, 3 Avenue Circulaire, 1180 Brussels, Belgium*

^d*Department of Aerospace Engineering, Auburn University, Auburn, AL 36849, USA*

^e*Department of Geosciences, Auburn University, Auburn, AL 36849, USA*

ARTICLE INFO

Keywords:

Asteroids, dynamics
Satellites of asteroids
Tides, solid body
Near-Earth objects

ABSTRACT

Synchronous binary asteroids can experience libration about their tidally-locked equilibrium, which will result in energy dissipation. This is an important topic to the Asteroid Impact and Deflection Assessment, where excitation caused by the DART kinetic impact in the Didymos binary asteroid system may be reduced through dissipation before Hera arrives to survey the effects of the impact. We develop a numeric model for energy dissipation in binary asteroids to explore how different system configurations affect the rate of energy dissipation. We find tumbling within the synchronous state eliminates a systematic trend in libration damping on short timescales (several years), but not over long times (hundreds of years) depending on the material conditions. Furthermore, damping of libration, eccentricity, and fluctuations in the semimajor axis are primarily dependent on the stiffness of the secondary, whereas the semimajor axis secular expansion rate is dictated by the stiffness of the primary, as expected. Systems experiencing stable planar libration in the secondary can see a noticeable reduction in libration amplitude after only a few years depending on the stiffness of the secondary, and thus dissipation should be considered during Hera's survey of Didymos. For a very dissipative secondary undergoing stable libration, Hera may be able to calculate the rate of libration damping in Dimorphos and therefore constrain its tidal parameters.

1. Introduction

The Asteroid Impact and Deflection Assessment (AIDA) is a collaboration supported by NASA and ESA to test the feasibility of a kinetic impactor to deflect a small asteroid for the purpose of planetary defense (Cheng et al., 2018). Two missions will combine results to produce the most accurate knowledge possible on the first kinetic impact of an asteroid: NASA's DART (Double Asteroid Redirection Test), which will perform the actual kinetic impact (Rivkin et al., 2021), and ESA's Hera, which will assess the effectiveness of the impact several years later (Michel et al., 2022). The target of the impact is Dimorphos, the secondary in the Didymos binary asteroid system. By impacting Dimorphos, DART will change the mutual orbit period around Didymos, and ground-based measurements of the orbit period change will reveal how much momentum was transferred to Dimorphos. Approximately 4 years after the DART impact, Hera is scheduled to rendezvous with the Didymos system to perform a detailed analysis of the post-impact system, making several key measurements.

The degree to which the system's dynamics will evolve through energy dissipation between the DART impact and Hera's arrival remains an open question for AIDA. While this window is only around 4 years, a rubble-pile structure – like Didymos is hypothesized to be based on earlier dynam-

ics and geological studies (Agrusa et al., 2022; Walsh, 2018; Walsh et al., 2008; Jacobson and Scheeres, 2011a) – may be very efficient at dissipating energy, and thus this problem warrants attention. The question of energy dissipation after the DART impact and prior to Hera's rendezvous with Didymos is necessary in order to maximize the scientific and practical return of the AIDA collaboration. As Hera characterizes the spin state of Dimorphos, it is important to understand how the current spin state has changed since the impact in order to fully comprehend the effects of the DART impact. Ignoring dissipation in the system may lead to an incorrect estimation of the efficacy of a kinetic impactor during Hera's survey. While the scientific implications of this work extend beyond AIDA and Didymos to binary asteroid dynamics in general, we focus our analysis to this application given its current relevance and the wealth of analysis on Didymos and the DART impact in the literature.

While binary asteroids provide an ideal test site for planetary defense missions given their short mutual orbit periods (Cheng et al., 2018), they also offer a chance to study the unique dynamics of the full 2-body problem (F2BP). Given the asteroids' close proximity and generally asymmetric shapes (Pravec et al., 2016), their orbital motion is strongly coupled with their attitude, leading to complex dynamics (Maciejewski, 1995; Scheeres, 2006, 2009). Through this strong coupling, the bodies' spins and mutual orbit will evolve concurrently while energy dissipation occurs. Additionally, spin-orbit coupling can lead to attitude instabilities as a result of orbit perturbations such as the DART impact (Agrusa et al., 2021).

There are two main mechanisms of energy dissipation

*Corresponding author at 3775 Discovery Dr, Boulder, CO 80303, USA

E-mail address: alex.meyer@colorado.edu

ORCID(s): 0000-0001-8437-1076 (A.J. Meyer); 0000-0002-3544-298X (H.F. Agrusa); 0000-0002-1649-7176 (G. Noiset); 0000-0002-1821-5689 (M. Hirabayashi); 0000-0002-9840-2416 (R. Nakano)

we will consider in this work, both stemming from the deformation of the bodies. The first is tidal torque, in which the tidal forces of both bodies act to move the system into a synchronous equilibrium (Murray and Dermott, 1999; Goldreich and Sari, 2009; Taylor and Margot, 2010). The second is non-principal axis (NPA) rotation, in which rotation about any axis other than the major principal axis will dissipate energy until the major principal axis is aligned with the angular momentum (Burns et al., 1973; Breiter et al., 2012; Molina et al., 2003; Ershkov and Leshchenko, 2019; Pravec et al., 2005). Both these mechanisms will drive the system toward a configuration in which the two asteroids are mutually tidally locked, with their spin angular momentum vectors aligned with their major principal axes and the orbit angular momentum vector (Taylor and Margot, 2011). We call this state the doubly-synchronous equilibrium.

While many studies focus on energy dissipation in the two-body problem, they generally ignore the specific dynamical regime that Didymos will inhabit after the DART impact: a system which is generally synchronous but with nonzero libration of the secondary (Taylor and Margot, 2010; Goldreich and Sari, 2009). Here we define libration as any angular deviation of the secondary's long axis away from the tidally locked configuration, but smaller than 90° so the secondary remains on-average synchronous. Generally there are two modes of libration: free and forced (Murray and Dermott, 1999). While forced libration is driven by eccentricity, free libration is governed by the average libration over an orbit period and is thus eccentricity-agnostic (Tiscareno et al., 2009). Given the strongly coupled nature of binary asteroids, we make no distinction between these two modes and simply adopt the physical libration angle. This study will focus exclusively on this dynamic state and so also carries scientific merit beyond the specific application of the AIDA collaboration. More recently, Efroimsky (2018) analyzed energy dissipation in a tidally perturbed librating body. This is the same regime we are interested in here, but we attempt to relax the small-libration assumption from that work and extend results to binary asteroids, which orbit much closer than planet-moon systems. Another noteworthy study is that of Jacobson and Scheeres (2011a), who apply a tidal torque model to binary asteroids. However, this analysis is limited to 2 dimensions, whereas we are interested in the full 3 dimensional dynamics. Quillen et al. (2020, 2022) study tidal dissipation in coupled systems with some attention spent on the libration state, and our work falls in a similar vein but we focus on how different shapes and stiffness of the secondary affect the dissipation process.

Since the main motivation of this study is the AIDA collaboration, we first provide background on Didymos, the DART impact, and previous analyses on the post-impact dynamics in Section 2. We then derive our dynamical model, including dissipation mechanisms, in Section 3. Results on energy dissipation are presented in Section 4, and we validate these results by comparing with a higher-fidelity numeric model in Section 5. The implications for Hera over the short-term are investigated in Section 6. In Section 7 we discuss the

possible implications of the BYORP effect, and in Section 8 we investigate how the dissipation behavior depends on the material parameters. Finally, we present a discussion and our conclusions in Section 9.

2. Background

We will apply our dissipation model to the Didymos system, which we nominally assume is in a singly-synchronous equilibrium prior to any perturbation, with the secondary's rotation period equal to the orbit period. The rationale for this assumption is outlined in Richardson et al. (2022). To calculate this equilibrium we adopt the method described in Agrusa et al. (2021) and iterate the system bulk density until the stroboscopic orbit period matches the observed value. We define the stroboscopic orbit period as the time required for the secondary to traverse 360° relative to an inertial observer, akin to a lightcurve observation. This approach means we have developed our own independent estimate of the system density rather than using values derived from observations, although our density lies within the error bars of the observed value (Naidu et al., 2020; Scheirich and Pravec, 2022). We calculate the stroboscopic orbit period using the method outlined in Meyer et al. (2021). The resulting equilibrium system has the parameters outlined in Table 1. We will assume a triaxial shape for the secondary, but note changing the axis ratios of Dimorphos does not appreciably affect the equilibrium parameters of the system. While keeping the mean radius of Dimorphos constant, we will vary its axis ratios (a/b and b/c , with $a > b > c$) to investigate how the shape of Dimorphos affects the energy dissipation rate.

In this work we will focus on two shapes of the secondary, one with $a/b = 1.2$, $b/c = 1.1$, and the other with $a/b = 1.4$, $b/c = 1.3$. In conjunction with the mean radius, we can solve for the semiaxes that define the ellipsoid, as well as the dimensionless shape parameter S defined as

$$S = \frac{B - A}{C} \quad (1)$$

where A , B , and C are the three principal moments of inertia of the ellipsoid corresponding to the axes a , b , and c , respectively. Table 2 gives the dimensions of the two ellipsoids we will primarily use as Dimorphos, as well as their shape parameter S .

The DART impact will push Dimorphos out of the equilibrium state (Meyer et al., 2021; Agrusa et al., 2021). The impact can be quantified by the momentum enhancement factor known as β , which is defined as the ratio of the true system momentum change to the momentum carried by the impactor. Mathematically, this is described as

$$\beta = \frac{P_{\text{true}}}{P_{\text{impactor}}} \quad (2)$$

β can be converted into a change in velocity using the relationship

$$\Delta \vec{v} = \frac{M_{\text{impactor}}}{M_B} (\vec{u} + (\beta - 1) (\hat{u} \cdot \vec{u}) \hat{n}) \quad (3)$$

Table 1

Summary of the equilibrium Didymos system prior to the DART impact, from Pravec et al. (2022), Scheirich and Pravec (2022), Naidu et al. (2020), and Scheirich and Pravec (2009). Our density estimate differs from that reported in Scheirich and Pravec (2022) as we calculate it using a dynamical approach, but our solution falls within the 1σ derived error bars.

Parameter	Symbol	Value	Notes
Orbit Period	P_{orb}	11.92 hr	Measured (Pravec et al., 2022; Scheirich and Pravec, 2022)
Didymos Rotation Period	P_A	2.26 hr	Measured (Pravec et al., 2022)
Didymos Mean Radius	R_A	390 m	Derived (Naidu et al., 2020)
Dimorphos Mean Radius	R_B	82 m	Derived (Naidu et al., 2020; Scheirich and Pravec, 2009)
System Bulk Density	ρ	2.2 g/cm ³	Derived here, similar to (Scheirich and Pravec, 2022)
Semimajor Axis	a	1200 m	Measured (Naidu et al., 2020)
Eccentricity	e	0	Assumed (Scheirich and Pravec, 2022; Richardson et al., 2022)
Inclination	i	0°	Assumed (Scheirich and Pravec, 2022; Richardson et al., 2022)

Table 2

Summary of the two triaxial ellipsoids used throughout this work as the secondary shape.

Shape	a [m]	b [m]	c [m]	S
$a/b = 1.2, b/c = 1.1$	95.6	79.7	72.4	0.18
$a/b = 1.4, b/c = 1.3$	112	80.0	61.5	0.32

where $M_{impactor}$ is the impactor mass, M_B is the mass of Dimorphos, \vec{u} is the impactor velocity, and \hat{n} is the outward surface normal at the impact site (Rivkin et al., 2021; Feldhacker et al., 2017). For this analysis we will assume \hat{n} is parallel to the velocity of Dimorphos, and that \vec{u} is misaligned with the velocity vector by 10 degrees out of the orbit plane and 10 degrees in the radial direction, consistent with Richardson et al. (2022). Note the impact is retrograde, decreasing the mutual orbit period while increasing its eccentricity. From Richardson et al. (2022), we use an impactor mass of 536 kg and velocity of 6.143 km/s relative to the secondary.

For this analysis, we will assume a perturbation equivalent to a β value of 3, as this is large enough to excite unstable motion in some shapes of Dimorphos, but small enough to allow stable motion in other shapes, and also lies in the expected range of β : $1 < \beta \lesssim 6$ (Raducan and Jutzi, 2022; Stickle et al., 2022). A perturbation of $\beta = 3$ is roughly equivalent to increasing the eccentricity to around 0.02, depending on the secondary shape and mass. This allows us to study both stable and unstable dynamical regimes without having to test multiple perturbation magnitudes. Note this selection is not grounded in the actual DART impact, as we are interested in how different secondary shapes affect dissipation rates within a system rather than making any quantitative predictions, as an accurate prediction is impossible without knowledge of the system's interior structure. Following the DART impact and Hera survey, this analysis can be revisited with better constraints on the shape and mass of Dimorphos. We reproduce the results of Agrusa et al. (2021) for $\beta = 3$ in Fig. 1 to show the unstable region of motion.

While the size of Dimorphos is fixed by the bulk diameter, the shape of the triaxial ellipsoid is defined by the axis ratios a/b and b/c , where a , b , and c are the longest, intermediate, and shortest semiaxes of the ellipsoid, respectively. Fig. 1 shows the amplitude of the 1-2-3 Euler angles, corresponding to roll, pitch, and yaw, for each secondary shape. If a system is in a true equilibrium, these angles would remain zero. An unstable region is apparent in Fig. 1 where some secondary shapes result in tumbling. The unstable region in which the secondary begins to tumble is outlined by a yellow dashed line. This is not a formal boundary for this region and is only intended to aid interpretation. The unstable region is dependent on the system's eccentricity, so this boundary can not be applied outside of our impact scenario.

Due to the spin-orbit coupling in binary asteroids, these systems are non-Keplerian, and thus osculating Keplerian elements can be somewhat misleading. In an equilibrium configuration, the secondary may appear to be in a circular orbit to an external observer, but the Keplerian orbit is elliptical. In this configuration, the secondary is trapped at periapsis while the orbit itself precesses. Thus, there is a non-zero eccentricity at equilibrium and the semimajor axis is not the same as the separation distance (Scheeres, 2009). However, these elements are still useful as they can give us an idea of the system's secular evolution over time, and we use the Keplerian osculating elements throughout this work.

3. Dynamical Model

The mutual dynamics of binary asteroids are characterized by the F2BP, in which the orbit and attitude of the bodies are coupled. This leads to complex dynamics, and various models have been developed to simulate these systems with varying trade-offs between fidelity and computational cost. Since we are concerned with timespans of many years, it is necessary to select a more basic model at the cost of reduced fidelity. In this context, we are more concerned with the system's qualitative behavior over long time periods rather than short-term accuracy, so this is a fine compromise. As such, we model Didymos as a spherical primary and Dimorphos as

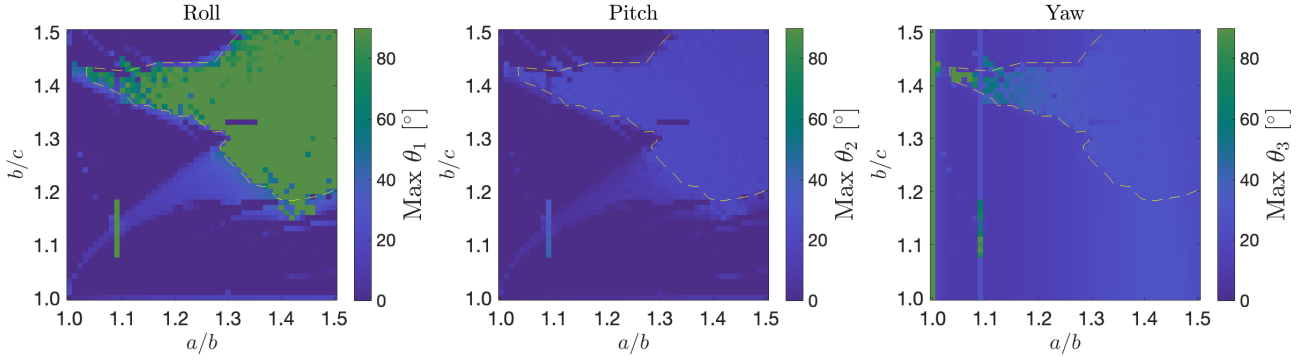


Figure 1: The maximum amplitude of the 1-2-3 Euler angles for an impact corresponding to $\beta = 3$ ($e \approx 0.02$), from the simulation set from Agrusa et al. (2021). The unstable regions, indicated by nonzero amplitudes in the roll and pitch angles, are governed by intersections of various resonances among fundamental frequencies of the system. The unstable region is outlined by the yellow dashed line; this is not a formal boundary and only serves to aid interpretation.

an ellipsoidal secondary, which allows for full 3D dynamics with an elongated secondary without becoming too computationally expensive. We will validate this model against a high-fidelity model in Section 5. Fig. 2 shows a diagram of the system, where body A is Didymos and body B is Dimorphos. In later discussions, quantities with subscripts A or B specify those for the designated bodies.

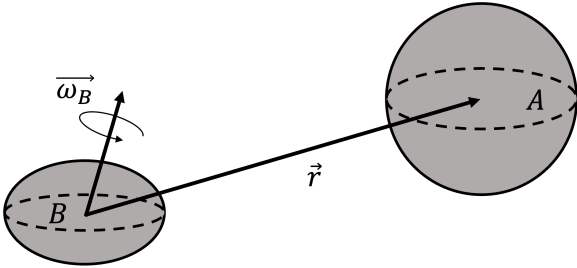


Figure 2: Diagram showing the dynamic model.

The equations of motion are straightforward and we omit any derivation, instead referring the reader to Scheeres (2006). These equations are defined in the body-fixed frame of the secondary. We have six degrees of freedom, being the relative separation and the rotation of Dimorphos. The equations of motions are

$$\ddot{\vec{r}} + 2\dot{\vec{\omega}}_B \times \dot{\vec{r}} + \dot{\vec{\omega}}_B \times \vec{r} + \vec{\omega}_B \times (\vec{\omega}_B \times \vec{r}) = \mathcal{G}(M_A + M_B) \frac{\partial U}{\partial \vec{r}} \quad (4)$$

$$\mathbf{I}_B \cdot \dot{\vec{\omega}}_B + \vec{\omega}_B \times \mathbf{I}_B \cdot \vec{\omega}_B = -\mathcal{G}M_A M_B \vec{r} \times \frac{\partial U}{\partial \vec{r}} \quad (5)$$

where \mathbf{I}_B is the inertia tensor of the secondary, which is a simple diagonal matrix in the secondary's body-fixed frame. U is the gravitational potential around the ellipsoidal Dimorphos, and to ease computation time we use a second degree expansion in the form of MacCullagh's formula (Murray and

Dermott, 1999):

$$U = -\frac{\mathcal{G}M_A M_B}{r} - \frac{\mathcal{G}M_A(A + B + C - 3\Phi)}{2r^3} \quad (6)$$

where A , B , and C are respectively the minimum, intermediate, and maximum principal inertia values of Dimorphos, and Φ is a quantity defined by

$$\Phi = \frac{Ax^2 + By^2 + Cz^2}{r^2} \quad (7)$$

with (x, y, z) being the Cartesian coordinates of the primary in the secondary's body-fixed frame so that $\vec{r} = x\hat{i} + y\hat{j} + z\hat{k}$.

We next need to introduce the methods of dissipation through non-rigid processes, both through tidal torque and NPA rotation, which rise from a combination of deformation, rotation, and translation of the bodies (Hirabayashi, 2022). We ignore any surface motion on both the primary and secondary, which includes rotation-induced granular motion on the secondary's surface and any associated body reshaping, which changes the gravitational potential energy (Agrusa et al., 2022; Agrusa et al., 2022), tidal saltation and YORP-induced landslides on the primary (Harris et al., 2009), and boulder movement on either body (Brack and McMahon, 2019), which would also dissipate energy. We will assume any reshaping and surface motion to be small and intermittent, and the energy dissipated by these events to be negligible over time. So our estimates on damping times for Didymos can be considered conservative for a given set of material properties since additional mechanisms will only increase the dissipation rate.

3.1. Tidal Torque

To describe energy dissipation from the system, we introduce equations for tidal torque to add to our dynamic model. In selecting a basic model for tidal torque, we have two choices: the constant Q model, in which the rate of dissipation is driven by the ratio of tidal quality factor Q and the simple

Love number k_2 (Murray and Dermott, 1999), or the constant time lag model, in which the angle between the tidal bulge and the line connecting the two bodies is a constant Δt (Mignard, 1979; Hut, 1981). Based on the physics of our problem setup, the secondary will librate about the synchronous configuration, and thus a constant lag angle would be inappropriate, as the lag angle should oscillate as a result of the libration. For this reason we select the constant Q model, which is the same model adopted by Jacobson and Scheeres (2011a), in which the tidal torque is defined as:

$$\Gamma = -\text{sign}(\omega - \omega_{orb}) \frac{3}{2} \left(\frac{3}{4\pi\rho} \right)^2 \frac{GM_A^2 M_B^2 k}{r^6 R Q} \quad (8)$$

where the body's angular velocity is ω , the orbit's angular rate is ω_{orb} , R is the reference radius for the body, ρ is its density, and Q/k is the tidal dissipation ratio. The tidal quality factor Q is related to the tidal bulge lag angle ($Q \sim 1/\sin \epsilon$), while the love number k_2 describes the level of body deformation due to the tidal potential. Henceforth we drop the subscript 2 on the Love number for simplicity. A large value of Q/k corresponds to a more stiff body that dissipates more slowly. In reality, the tidal dissipation is far more complicated than simply selecting constant values for the unknown Q/k values. As pointed out by Efroimsky (2015), tidal dissipation in binary asteroids, including rubble piles, may be governed primarily by the body's viscosity, rather than rigidity. Others, including Goldreich and Sari (2009) and Nimmo and Matsuyama (2019), argue that friction is a critical parameter. Since there is no current estimate for the viscosity of rubble pile asteroids to the authors' knowledge, we adopt the friction approach. Furthermore, while many studies assume the quality number Q to be constant, this parameter depends on the tidal frequency. Further complicating this relationship is the fact that the tidal quality number is not a linear function of the tidal frequency, and can either increase or decrease with the frequency (Ferraz-Mello, 2013). We also are left with the problem of the tidal lag angle oscillation. To address this we adopt the same solution as Jacobson and Scheeres (2011a); we will linearize the tidal torque around the point where $(\omega - \omega_{orb})$ is near zero so the torque does not immediately switch signs as the secondary librates (see Appendix C therein for details on this linearization). This linearization is necessary, as the tidal bulge is a physical phenomenon and requires a finite time to cross between leading or trailing the tide-raising body.

Note that Taylor and Margot (2010) point out the simple tidal model assumes the two bodies are widely separated, whereas the separation between Didymos and Dimorphos is only slightly larger than 3 primary radii. In their work, Taylor and Margot (2010) calculate that higher order terms in the tidal potential speed up the process of tidal evolution. However, they also find that uncertainties in the system, particularly surrounding Q/k , dominate over the higher order tidal expansion. Thus, we continue with the simple tidal model given the large uncertainty associated with the bulk system density and physical properties, while keeping in mind higher order terms in the tidal model will only in-

crease the rate of damping in the system. Thus, the error associated with this tidal model is considered to be secondary to the considerable uncertainty on the Q/k coefficient for our purposes.

Unfortunately, given the lack of knowledge on the physical parameters of rubble piles, particularly their viscosity, we cannot calculate an accurate value for Q/k . For lack of a better option, we surrender ourselves to the typical simplifications surrounding the factor Q/k , and we turn to the work by Nimmo and Matsuyama (2019), who derive an estimate for a constant Q/k for rubble pile binary asteroids, which can be approximated by

$$\frac{Q}{k} \approx 300R \quad (9)$$

for R in meters. This leads to a value for the primary $Q_A/k_A \approx 1 \times 10^5$ and for the secondary $Q_B/k_B \approx 2.5 \times 10^4$. Note this expression for Q is frequency dependent and derived for a non-synchronous binary system. However, we again emphasize there is large uncertainty associated with these values so this definition serves as a first-order approximation, as the error from uncertainties dominates over the error from the assumptions. Furthermore, these values are consistent with existing estimates for small bodies in the literature (Brasser, 2020; Jacobson and Scheeres, 2011b; Scheirich et al., 2015, 2021). However, there is not a consensus on this linear scaling. For example, Goldreich and Sari (2009) propose an inverse scaling of Q/k with R , and even in their own work Nimmo and Matsuyama (2019) point out a scaling with $R^{3/2}$ may be more accurate. Another consideration is if Dimorphos turns out to be monolithic instead of a rubble pile, its Q/k value would likely be orders of magnitude higher (Goldreich and Sari, 2009). Hence, the large uncertainty in Q/k dominates over other errors associated with our model, and it is futile to develop a high fidelity tidal model while limited by this unknown parameter. Given the large uncertainty and lack of consensus around Q/k , we adopt the linear scaling only as nominal parameters, and subsequently investigate how varying Q/k for both the primary and secondary affects the system behavior later in Section 8.

Returning to the tidal torque equation, this model is still only defined in 2-dimensions and we wish to extend this to a full 3-dimensional analysis, as out-of-plane rotation of the secondary is a possibility. This can be done with only a few corrections to the classic model. To start, we need to define a vector for the torque direction. The torque will act to push the spin rates of the asteroids into the synchronous equilibrium, but physically cannot act in the direction of the position vector of the secondary relative to the primary. We define the relative spin rate of a body:

$$\dot{\phi} = \vec{\omega} - \vec{\omega}_{orb} \quad (10)$$

We can then use this spin vector as the vector along which the torque acts, with a small correction so the torque in the radial direction is zero:

$$\hat{\Gamma} = - \frac{\dot{\phi} - (\dot{\phi} \cdot \hat{r})\hat{r}}{|\dot{\phi} - (\dot{\phi} \cdot \hat{r})\hat{r}|} \quad (11)$$

This formulation also takes care of the sign of the torque, as the torque will generally act in the direction opposite the relative spin rate, so that a secondary rotating faster than the orbit rate is slowed, while a secondary rotating slower will be sped up. Furthermore, any out-of-plane rotation is countered by the torque, with the exception of any spin about the relative position vector, as tidal torque can only act perpendicular to this direction. Thus, we don't need any further consideration on the sign of the torque and can remove the $-\text{sign}(\omega - \omega_{orb})$ expression from Eq. 8 and substitute Eq. 11 in its place.

While we formulated the 3D torque expression with the secondary in mind, it is also equally applicable to the primary, as tidal dissipation will ultimately drive the system to the doubly synchronous state. So we have developed expressions for the torque on both bodies. However, to accurately express the equations of motion we also need to consider the torque on the orbit. By the conservation of angular momentum, the torque on the orbit is simply

$$\vec{\Gamma}_{orb} = -(\vec{\Gamma}_A + \vec{\Gamma}_B). \quad (12)$$

However, to include this in the orbital equation of motion we will need to calculate this torque's effect on $\ddot{\vec{r}}$. Turning to the orbital angular momentum we know

$$\dot{\vec{H}} = \frac{d}{dt}(m\vec{r} \times \dot{\vec{r}}) = \vec{\Gamma}_{orb} \quad (13)$$

where $m = \frac{M_A M_B}{M_A + M_B}$. This gives

$$m\vec{r} \times \ddot{\vec{r}} = \vec{\Gamma}_{orb}. \quad (14)$$

We would like to solve this equation for $\ddot{\vec{r}}$ to update the orbital equation of motion with the tidal torque. We note that

$$\vec{r} \times (\vec{r} \times \ddot{\vec{r}}) = (\vec{r} \cdot \ddot{\vec{r}})\vec{r} - (\vec{r} \cdot \vec{r})\ddot{\vec{r}} = \vec{r} \times \frac{\vec{\Gamma}_{orb}}{m} \quad (15)$$

which can be arranged to find:

$$\ddot{\vec{r}} = \frac{\vec{\Gamma}_{orb} \times \vec{r}}{mr^2} + \frac{\vec{r} \cdot \ddot{\vec{r}}}{r^2} \vec{r}. \quad (16)$$

However, this is not a unique solution, as for any real number K we can find

$$\ddot{\vec{r}} = \frac{\vec{\Gamma}_{orb} \times \vec{r}}{mr^2} + K \frac{\vec{r} \cdot \ddot{\vec{r}}}{r^2} \vec{r} \quad (17)$$

is also a valid solution as a result of the dot product. Thus, we must solve the problem of a non-unique solution. We note that whenever the torque $\vec{\Gamma}_{orb}$ is equal to zero, there should be no contribution to the equation of motion. So we choose $K = 0$ to enforce this constraint (alternatively, we force the acceleration to be perpendicular to the position vector, so that $\vec{r} \cdot \ddot{\vec{r}} = 0$), and we are left with

$$\ddot{\vec{r}} = \frac{\vec{\Gamma}_{orb} \times \vec{r}}{mr^2} = \vec{\gamma}_{orb}. \quad (18)$$

where we introduce the term $\vec{\gamma}_{orb}$ as the acceleration due to the torque on the orbit. This makes sense given the physical context, where the tides should not have any effect in the radial direction. Note that this formula must be calculated in an inertial frame as it is derived from the orbit angular momentum. Once computed in an inertial frame, it can be transformed into the secondary body-fixed frame for use in the equations of motion.

3.2. NPA Rotation

Any NPA rotation of the secondary will act to dissipate energy while keeping its angular momentum constant, until its maximum principal inertia axis is aligned with its angular momentum. There is a wide variety of work that has considered this problem (Burns et al., 1973; Molina et al., 2003; Pravec et al., 2005; Ershkov and Leshchenko, 2019), but for the most applicable to this work we turn to Breiter et al. (2012), who calculate the rate of energy dissipation in a triaxial ellipsoid rotating in either long-axis mode or short-axis mode. The full expression for energy dissipation in a triaxial ellipsoid undergoing NPA rotation is quite complicated, and we report a condensed version here:

$$\dot{E}_{NPA} = \frac{a^4 \rho M_B \bar{\omega}_B^5}{\mu Q} \Psi \quad (19)$$

where a is the secondary's longest semiaxis, $\bar{\omega}_B$ is its nominal rotation rate, and Ψ is a complicated function of the secondary's shape, Poisson's ratio, and an elliptic modulus. We omit the details here and refer the reader to Breiter et al. (2012), for the full expression. This expression uses the Lamé constant μ instead of the Love number k , but we can relate our Q/k to μQ through (Murray and Dermott, 1999; Nimmo and Matsuyama, 2019):

$$\mu Q \sim \mathcal{G} \frac{Q}{k} \rho^2 R^2. \quad (20)$$

At the risk of sounding repetitive, we again highlight the shortfall of this relationship as pointed out by Efroimsky (2015), as Q is frequency dependent. Thus, the Q selected for the tidal dissipation model is not necessarily the same Q for NPA rotation, again introducing considerable uncertainty. However, we assume the driving frequencies for tidal and NPA dissipation are the same, and again for lack of a better option we adopt the same Q for both methods of dissipation.

Since the equations of motion are defined in the secondary's body-fixed frame, the energy dissipation due to NPA rotation will apply an 'effective torque' to rotate the secondary's angular momentum to align it with its maximum principal inertia axis while keeping the magnitude constant.

To obtain the effective torque, we start with the energy dissipation equation

$$\dot{E} = \vec{\omega}_B \cdot I_B \dot{\vec{\omega}}_B. \quad (21)$$

Next, we expand the equation $\dot{\vec{H}}_B = \vec{\Gamma}_{NPA}$ for secondary angular momentum H_B :

$$\vec{\Gamma}_{NPA} = I_B \dot{\vec{\omega}}_B + \vec{\omega}_B \times I_B \vec{\omega}_B. \quad (22)$$

By taking the dot product of this equation with $\vec{\omega}_B$, we can find an expression for the effective torque as a function of \dot{E} :

$$\vec{\omega}_B \cdot \vec{\Gamma}_{NPA} = \dot{E}_{NPA}. \quad (23)$$

Of course, due to the dot product, this is not a complete expression as we still need to define the direction of the effective torque $\vec{\Gamma}_{NPA}$. Since NPA dissipation will not change the angular momentum magnitude, only the angular momentum's direction relative to the body-fixed axes of the secondary, the effective torque must be perpendicular to the angular momentum. As a conceptual illustration, imagine a satellite undergoing torque-free tumbling. In this scenario, the satellite's angular momentum vector is constant, while dissipation reorients the satellite so that its principal axis is aligned with the angular momentum (and its kinetic energy is minimized). In the same sense, within the body-fixed frame of the secondary, its angular momentum will appear to rotate until it is aligned with the principal axis, while maintaining a constant magnitude. This is accomplished by applying an effective torque perpendicular to the angular momentum, such that this torque only rotates the angular momentum vector, but does not scale it. We define an intermediate vector

$$\vec{k} = \vec{H}_B \times \hat{z} \quad (24)$$

where \hat{z} is the secondary's maximum principal inertia axis. We then use this intermediate vector to define the torque unit vector

$$\hat{\Gamma} = \frac{\vec{H}_B \times \vec{k}}{|\vec{H}_B \times \vec{k}|}. \quad (25)$$

The effective torque will act to rotate the angular momentum vector \vec{H}_B until it is aligned with the secondary's \hat{z} direction. The effective torque is then calculated as

$$\vec{\Gamma}_{NPA} = \frac{\dot{E}}{\vec{\omega}_B \cdot \hat{\Gamma}} \hat{\Gamma}. \quad (26)$$

Note that in reality, the secondary angular momentum vector will not rotate and instead the body-fixed coordinate axes of the secondary will rotate to align \hat{z} with the angular momentum vector. However, if we define our equations of motion in the secondary body-fixed frame as we have done, this effective torque will be appropriate to use.

3.3. Comparison

In order to compare our two methods of energy dissipation, we plot the rate of energy dissipation in the secondary as a function of the separation distance for a body rotating with a spin axis offset from its major principal axis by approximately 32° . This is near the switching point between long-axis and short-axis mode rotation, and thus NPA dissipation is near a maximum here. Fig. 3 shows the energy dissipation rates for the two mechanisms, highlighting that tidal dissipation is generally more than an order of magnitude stronger than NPA rotation for a close binary like Didymos. Despite this contrast, we still include the effects of

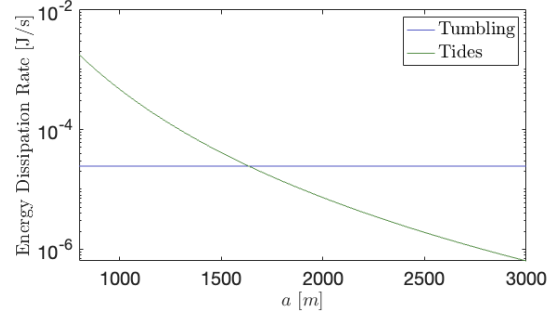


Figure 3: The rate of energy dissipation through tidal torque compared to NPA rotation as a function of separation. Tidal torque has orders of magnitude more of an effect than NPA rotation for a close binary system like Didymos.

NPA rotation as it does not significantly slow down the integration wall time.

While close systems like Didymos are dominated by tidal torque, wider systems see near-equal contributions from both tidal torque and NPA rotation, and NPA dissipation becomes dominant at very wide separations. The secondary shape and spin-axis obliquity will affect the rate of NPA rotation energy decay, but for Didymos the tidal torque will always be stronger owing to the close proximity of its secondary.

Looking at a system with a semimajor axis of 1200 m, we next examine how the secondary's spin offset angle affects dissipation. Fig. 4 shows the dissipation rate as a function of the angle between the secondary's spin axis and its principal moment of inertia axis (we call this angle δ , and a system with $\delta = 0^\circ$ is in principal axis spin). We see tidal dissipation is largely independent of the spin axis offset, but NPA rotation depends strongly on this angle. There is a discontinuity where the secondary switches from short-axis to long-axis mode rotation. Dissipation then quickly drops to zero as spin approaches either perfectly major ($\delta = 0^\circ$) or minor ($\delta = 90^\circ$) axis rotation.

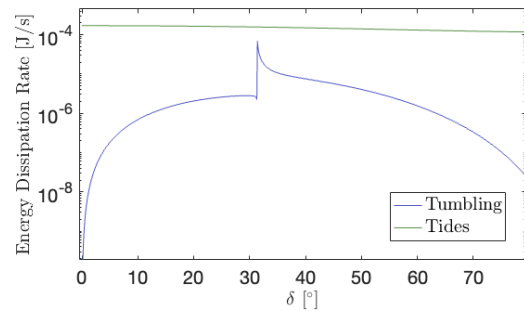


Figure 4: The rate of energy dissipation through tidal torque compared to NPA rotation as a function of secondary spin offset angle. The NPA dissipation is greatest near the discontinuity, where the secondary is switching between long-axis and short-axis rotation modes.

3.4. Equations of Motion

We can now add our dissipation mechanisms to our equations of motion, which will model the energy dissipation due to tides and NPA rotation while keeping the system's angular momentum constant:

$$\begin{aligned} \ddot{\vec{r}} + 2\vec{\omega}_B \times \dot{\vec{r}} + \dot{\vec{\omega}}_B \times \vec{r} + \vec{\omega}_B \times (\vec{\omega}_B \times \vec{r}) \\ = \mathcal{G}(M_A + M_B) \frac{\partial U}{\partial \vec{r}} + \vec{\gamma}_{orb} \end{aligned} \quad (27)$$

$$\mathbf{I}_B \cdot \dot{\vec{\omega}}_B + \vec{\omega}_B \times \mathbf{I}_B \cdot \vec{\omega}_B = -\mathcal{G}M_A M_B \vec{r} \times \frac{\partial U}{\partial \vec{r}} + \vec{\Gamma}_B + \vec{\Gamma}_{NPA}. \quad (28)$$

The uncoupled rotational dynamics equation of the spherical primary is simply

$$\mathbf{I}_A \dot{\vec{\omega}}_A = \vec{\Gamma}_A, \quad (29)$$

which is necessary to include to enforce the conservation of angular momentum.

For the sphere-ellipsoid model, we use a variable-step, variable-order Adams-Bashforth-Moulton predictor-corrector integrator to propagate the equations of motion. This integrator conserves the system energy (in the non-dissipative case) to within $5 \times 10^{-5}\%$ over 200 years. As an illustration, Fig. 5 shows the total system energy calculated by propagating the equations of motion using this integrator, for both the dissipative and non-dissipative cases. This demonstrates that the integrator conserves energy in the non-dissipative case and is accurate enough to capture the secular effects caused by energy dissipation.

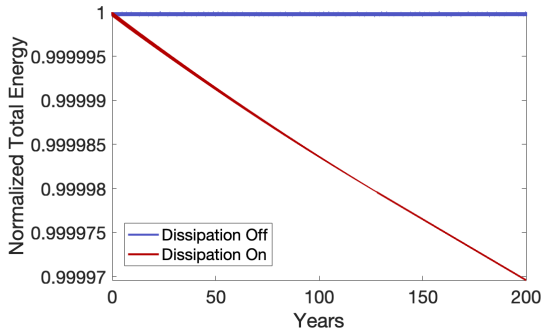


Figure 5: The total system energy, normalized by the initial energy, over 200 years comparing the dissipative to the non-dissipative case. This demonstrates the energy dissipation is a real effect and not caused by numerical error over this long time span.

4. Energy Dissipation

In investigating the energy dissipation of a librating binary asteroid, we must consider two dynamical regimes: stable libration or NPA rotation. A system in the stable regime will only see fluctuations in secondary rotation about its principal axis, whereas an unstable system will experience rotation about all three axes. For a uniform bulk density, the

dynamical regime of the system depends on the shape of the secondary, as illustrated in Fig. 1. We will select a system from both the stable and unstable region to carry out long-term simulations to investigate how a system dissipates its libration and returns to a synchronous equilibrium. For the stable system, we select a secondary with axis ratios $a/b = 1.2$, $b/c = 1.1$, and for the unstable system we choose $a/b = 1.4$, $b/c = 1.3$. Both of these shapes are within the predicted values for Dimorphos (Pravec et al., 2022). Note that energy dissipation in the primary is generally uniform across all shapes, so we thus exclude it from our analysis for simplicity.

4.1. Stable System

For the stable system, we simulate the dynamics for 200 years ($\sim 150,000$ orbit periods), during which the system returns to an equilibrium and begins to secularly evolve. We first examine the system energy, shown in Fig. 6. We plot the secondary rotational energy, the orbit energy, and the free energy. We define the free energy simply as the sum of the secondary rotational and orbit energies, or alternatively as the total energy sans the primary rotational energy. Since the primary rotational energy will uniformly decrease as a result of tides, the free energy is a better metric to examine the system's evolution. We see oscillations in the energy after the perturbation, which damp out as the system settles into a new equilibrium. Interestingly, the free energy decreases for a time before increasing. This indicates that dissipation acts to equilibrate the system faster than secularly evolve it. This is apparent in the exponential decrease in the secondary and orbit energy oscillations, as these values converge to a mean faster than the mean itself evolves.

This behavior is also apparent in Fig. 7, where we plot the Keplerian semimajor axis and eccentricity, along with the secondary libration angle. Again, we see the oscillations in the semimajor axis exponentially damping before any secular evolution is apparent. These oscillations damp at the same rate the eccentricity approaches its equilibrium value (recall that due to spin-orbit coupling, the equilibrium eccentricity is small but non-zero). This is also the same rate the libration damps to zero. In the libration angle we again see an initial exponential decrease.

As a result of spin-orbit coupling and the unique dynamics of binary asteroids, we see a new dynamical regime not previously studied in tidal analyses. It appears dissipation first acts to drive the system back toward an equilibrium by damping the eccentricity and oscillations in the system caused by libration, before the more classical secular tidal behavior is seen. Thus, rather than eccentricity and semimajor axis evolving concurrently as in classical tidal theory (e.g. Goldreich and Sari (2009)), the eccentricity is damped to a minimum before the semimajor axis evolves.

4.2. Unstable System

We next perform the same simulation for the unstable system. The system energy is shown in Fig. 8, where again we plot the secondary rotational energy, the orbit energy, and the free energy. Interestingly, on a comparable time scale as

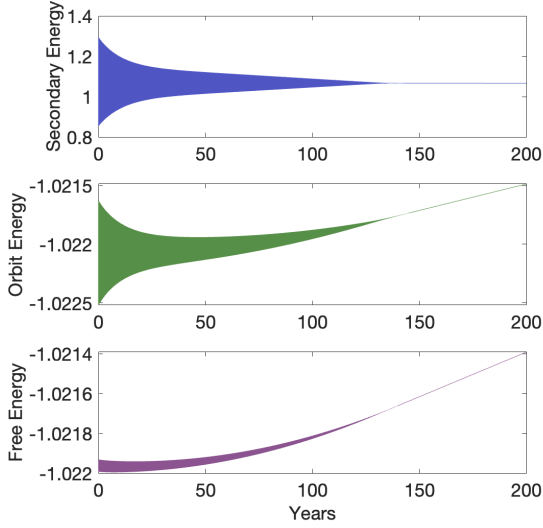


Figure 6: The secondary rotational energy (top), orbit energy (middle), and free energy (bottom) of the stable system with secondary $a/b = 1.2$, $b/c = 1.1$. The energies are normalized by the respective pre-impact equilibrium values. The oscillations within the energy are damped at the same rate across the secondary, orbit, and free energies. Here $Q_A/k_A \approx 1 \times 10^5$ and $Q_B/k_B \approx 2.5 \times 10^4$.

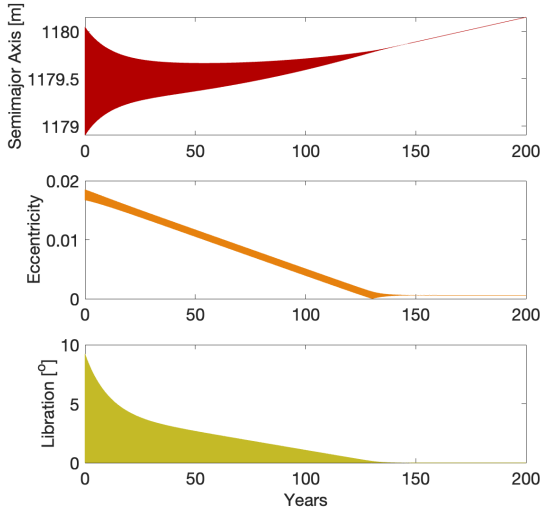


Figure 7: The Keplerian semimajor axis (top), eccentricity (middle), and libration angle (bottom) of the stable system with secondary $a/b = 1.2$, $b/c = 1.1$. The oscillations in semimajor axis and libration are damped at the same rate the eccentricity approaches its non-zero equilibrium value due to spin-orbit coupling. Here $Q_A/k_A \approx 1 \times 10^5$ and $Q_B/k_B \approx 2.5 \times 10^4$.

the stable system, the unstable system also returns to an equilibrium configuration. A notable difference is the oscillations in energy appear to converge linearly, unlike the stable system which experienced an exponential decay of oscillations. In the unstable system we again see an initial decrease in the free energy before it begins to increase as the orbit ex-

pands.

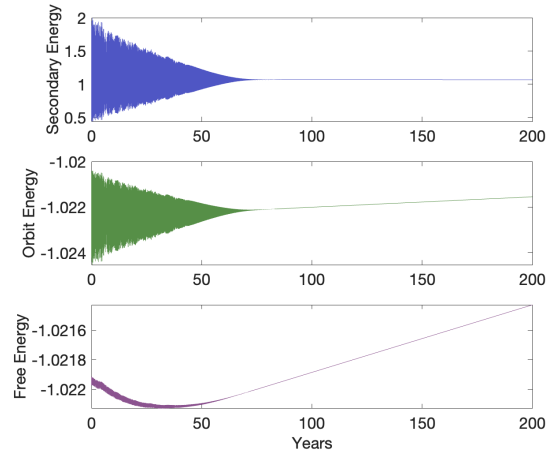


Figure 8: The secondary rotational energy (top), orbit energy (middle), and free energy (bottom) of the unstable system with secondary $a/b = 1.4$, $b/c = 1.3$. The energies are normalized by the respective pre-impact equilibrium values. The oscillations within the energy are damped at the same rate across the secondary, orbit, and free energies. Here $Q_A/k_A \approx 1 \times 10^5$ and $Q_B/k_B \approx 2.5 \times 10^4$.

In Fig. 9, we plot the semimajor axis, eccentricity, and libration angle of the unstable system. Again we see a linear, rather than exponential, decay in these elements. Once more, the timescale of damping is approximately uniform across all these elements, also consistent with the energy envelope decay times, highlighting the strength of the spin-orbit coupling. The binary asteroid cannot settle into an equilibrium while the libration amplitude is nonzero, or equivalently the eccentricity is not equal to its equilibrium value. This is consistent with the findings of Meyer et al. (2021), who point out the relationship between the secondary spin and the orbit oscillations.

An interesting takeaway from this result is both the stable and unstable systems reequilibrate on comparable timescales. While previous analyses have shown unstable rotation will slow dissipation (Wisdom et al., 1984; Quillen et al., 2022; Naidu and Margot, 2015), that applies to non-synchronous rotation, whereas our system never leaves an on-average synchronous configuration. Quillen et al. (2020) predict that tumbling within the synchronous state does not reduce energy dissipation and in fact can enhance it, and our results are consistent with that finding. However, a unique finding in our analysis is the close relationship between the eccentricity, libration, and oscillation within the semimajor axis. This is due to the spin-orbit coupling in binary asteroids, as any deviation from an equilibrium spin state of the secondary will also affect the orbit.

4.3. Analytic Models

An important question is how this numeric model compares to more classical analytic models of energy dissipation. Here, we focus only on tidal dissipation since this is

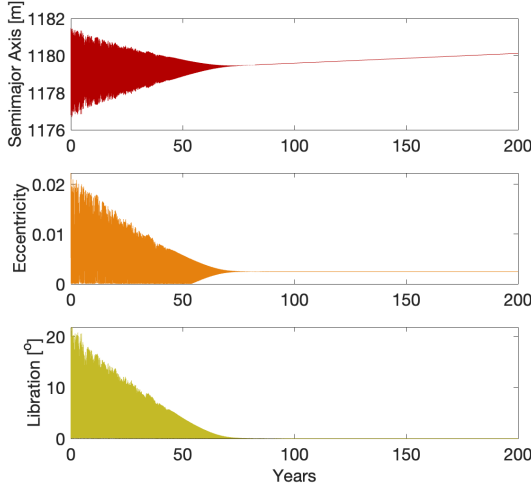


Figure 9: The semimajor axis (top), eccentricity (middle), and libration angle (bottom) of the unstable system with secondary $a/b = 1.4$, $b/c = 1.3$. The oscillations in semimajor axis and libration are damped at the same rate the eccentricity approaches its equilibrium value due to spin-orbit coupling. Here $Q_A/k_A \approx 1 \times 10^5$ and $Q_B/k_B \approx 2.5 \times 10^4$.

the dominant mechanism. Analytic equations for the evolution of semimajor axis and eccentricity of a binary system with $e \ll 1$ undergoing tidal dissipation are reported in Goldreich and Sari (2009):

$$\frac{\dot{a}}{a} = 3 \frac{k_A}{Q_A} \frac{M_B}{M_A} \left(\frac{R_A}{a} \right)^5 n \quad (30)$$

$$\frac{\dot{e}}{e} = \frac{57}{8} \frac{k_A}{Q_A} \frac{M_B}{M_A} \left(\frac{R_A}{a} \right)^5 n - \frac{21}{2} \frac{k_B}{Q_B} \frac{M_A}{M_B} \left(\frac{R_B}{a} \right)^5 n \quad (31)$$

where n is the mutual orbit mean angular velocity. Note in Eqs. 30 and 31, a refers to the binary mutual orbit semimajor axis rather than the secondary's longest semiaxis as used elsewhere in this work. In Eq. 31 for the eccentricity we see two terms: the first is the contribution from tides raised on the primary and the second is the contribution from tides raised on the secondary. The semimajor axis and eccentricity evolution is compared between the analytic model and our numeric results in Fig. 10 for the stable system and Fig. 11 for the unstable system.

For both the stable and unstable systems, the analytic model does a good job describing the secular rate of change of semimajor axis, but fails to account for the initial oscillations in semimajor axis. The analytic model also fails to describe the eccentricity damping rate and predicts a much slower decrease in eccentricity than what we see in our numeric model. These results make sense in the context of this problem; in our numeric model, the primary matches the assumptions in the analytic model: a rapidly rotating sphere. However, our secondary does not match the assumptions as it is neither spherical nor exactly tidally locked. Thus, we

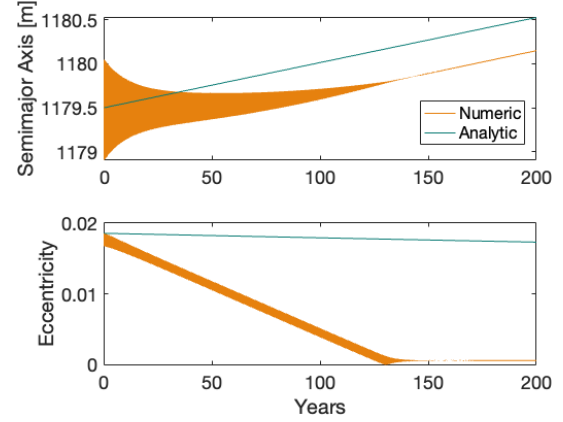


Figure 10: The semimajor axis (top) and eccentricity (bottom) for the stable system ($a/b = 1.2$, $b/c = 1.1$), comparing the numeric results to an analytic model. While the secular trend of semimajor axis is consistent between the models, the analytic model does a poor job of describing the eccentricity evolution.

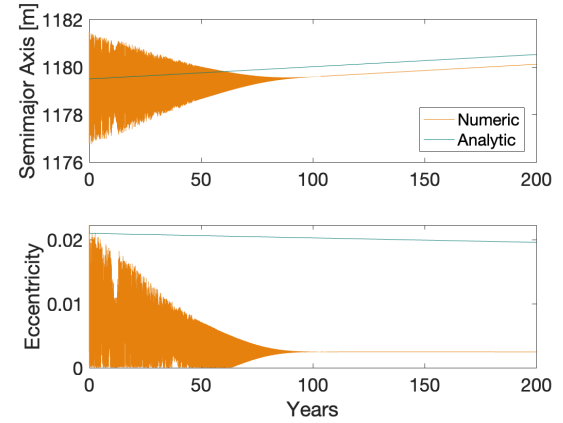


Figure 11: The semimajor axis (top) and eccentricity (bottom) for the unstable system ($a/b = 1.4$, $b/c = 1.3$), comparing the numeric results to an analytic model. While the secular trend of semimajor axis is consistent between the models, the analytic model does a poor job of describing the eccentricity evolution.

would expect to match the semimajor axis drift as this is driven by tides on the primary, but not the eccentricity damping rate, which has contributions from tides on the secondary. Furthermore, as the semimajor axis oscillations are driven by libration of the secondary, the analytic model does not capture this behavior. Note that our results have a non-negligible eccentricity, so we expect some error in the analytic model.

The analytic model of Goldreich and Sari (2009) makes no consideration of the secondary's libration. For this we turn to Jacobson et al. (2014) who develop an expression for

the damping rate of libration amplitude due to tides¹:

$$\dot{\Phi}_B = -\frac{k_B \omega_l \Phi_B^2}{Q S C \sin 2\Phi_B} \left(\frac{R_A}{\tilde{a}}\right)^3 \quad (32)$$

where the libration frequency ω_l is defined as

$$\omega_l = \frac{\pi \omega_d \sqrt{3S(1+s)}}{2K(\sin^2 \Phi_B)} \left(\frac{R_A}{\tilde{a}}\right)^{3/2}. \quad (33)$$

Here, $\omega_d = \sqrt{4\pi\rho G/3}$ is the spin disruption limit, $K(k^2)$ is the complete elliptic function of the first kind, $s = Cq^{2/3}(1+q)(R_A/\tilde{a})^2$ is the secondary perturbation term with mass fraction $q = m_B/m_A$. Here, \tilde{a} is the binary mutual orbit semimajor axis in units of the primary radius. $S = (B - A)/C$ is a shape parameter where $A < B < C$ are the dimensionless principal moments of inertia. For the derivation and in-depth discussion of this model we refer the reader to Jacobson et al. (2014).

While this formula is derived for a planar, circular orbit, it can still accurately be applied to our stable system as this remains essentially planar with a small eccentricity. We see in Fig. 12 that, for the stable system, there is good agreement between our numeric results and this analytic model. While the instantaneous dissipation rates can differ, the overall trend is similar and both models converge to zero in the same time frame. Applying this analytic model to the unstable system introduces error given the non-planar libration, but Fig. 13 still shows decent agreement. The biggest difference for the unstable system is the rate of dissipation, where the numeric model converges to zero faster than the analytic model. This indicates out-of-plane rotation of the secondary increases the rate of dissipation compared to purely planar libration, consistent with the findings of Quillen et al. (2020).

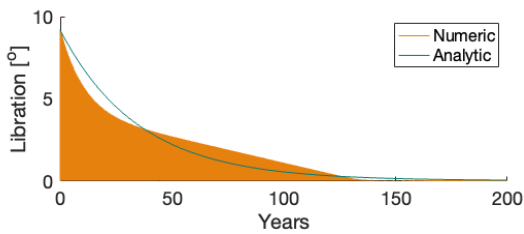


Figure 12: The libration amplitude for the stable system ($a/b = 1.2$, $b/c = 1.1$), comparing the numeric results to an analytic model. We see good agreement between the models, and both converge to zero on the same timescale.

While Jacobson et al. (2014) use the same equations as Goldreich and Sari (2009) for the orbit evolution (semimajor axis and eccentricity), their derivation of the libration damping rate sidesteps the problem with the eccentricity damping equation. Thus, the formula for libration damping gives a good approximation for the eccentricity damping since these quantities are closely related in the coupled problem. Of

¹The final result of this equation reported in Jacobson et al. (2014) is missing the $1/C$ term in the denominator.

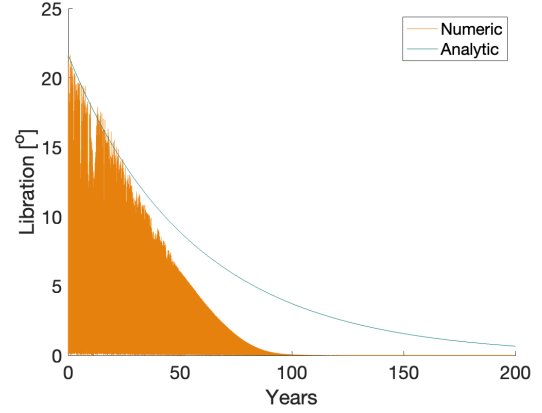


Figure 13: The libration amplitude for the unstable system ($a/b = 1.4$, $b/c = 1.3$), comparing the numeric results to an analytic model. The numeric model, experiencing non-planar libration, dissipates to zero faster than the analytic model predicts for planar libration.

course, this formula is more accurate for the stable, planar system. But a decent analytic approximation of the system's evolution can be made using only the semimajor axis and libration amplitude equations.

We have so far only compared two secondary shapes. These two shapes have a similar damping timescale, but additional tests are required to determine if this is a coincidence or a more general property. Fig. 30 in Appendix A compares the libration damping of six additional shapes of the secondary, and here we see across all 8 shapes tested the damping timescale is on the same order of magnitude regardless of the secondary's rotational stability.

5. Validation

While we have developed an efficient model for energy dissipation in two close rigid bodies, the sphere-ellipsoid model is simplistic and we must validate it against a higher-fidelity model. As a high-fidelity model, we use the General Use Binary Asteroid Simulator (GUBAS), which uses a fourth degree and order gravity field between two rigid bodies defined by polyhedral models (Davis and Scheeres, 2020, 2021). A fourth degree gravity expansion was previously found to accurately describe binary asteroid dynamics (Agrusa et al., 2020). While we use the polyhedral model for the Didymos primary, we continue using an ellipsoid secondary to test both stable ($a/b = 1.2$, $b/c = 1.1$) and unstable ($a/b = 1.4$, $b/c = 1.3$) systems. We have modified the GUBAS code to include the same tidal torque model as described in Section 3, but we do not include NPA rotation dissipation for efficiency as it is generally at least an order of magnitude smaller. We run these simulations for 5 years as this is generally long enough to compare trends, but longer simulations in GUBAS are prohibitively expensive to run.

In comparing these models, we use the set of 1-2-3 Euler angles (roll, pitch, yaw) to describe the secondary's orientation relative to the synchronous equilibrium. This allows for

a more accurate comparison than using only the physical libration angle.

5.1. Stable System

For the stable system, we first examine the energy, where Fig. 26 in Appendix A plots the secondary, orbit, and total energies. While, unsurprisingly, there are differences in the magnitudes of these quantities, their overall behavior is consistent. The rate of collapse of the secondary and orbit energies are similar between the models, and the secular trend of total energy is also consistent. There are larger oscillations in the total energy for the GUBAS model, but this is due to numerical noise, as the simplicity of the sphere-ellipsoid model allows us to use much tighter tolerances without a major sacrifice to computation cost.

We next examine the libration amplitude through 1-2-3 Euler angles (roll, pitch, yaw). Fig. 27 in Appendix A plots the 1-2-3 Euler angles for both the sphere-ellipsoid and GUBAS models, but θ_1 and θ_2 remain nearly zero due to the stable configuration. Again, there are small differences in the libration magnitude, but the damping rate is nearly identical between these models. One notable difference is it appears θ_1 and θ_2 , although nearly zero, only dissipate further in the sphere-ellipsoid model. However, we recall that the sphere-ellipsoid model uses a more stringent tolerance than GUBAS and we see less numeric noise (see Fig. 26). Thus, we expect when the out-of-plane angles are small enough as in this case, they will not further damp as a result of this numeric noise. Even in the sphere-ellipsoid model, the out-of-plane angles damp further but still do not reach exactly zero. The in-plane angle θ_3 , which has a significant amplitude, has a very strong agreement between the two models.

5.2. Unstable System

Next, we perform the same comparison for the unstable system. Fig. 28 in Appendix A plots the secondary, orbit, and total energy. Essentially, we see the same behavior as we did in the stable system, where there are clear, and expected, differences between the two models but the overall behaviors are very similar.

For the unstable system, where non-principal axis rotation is prevalent, we plot the 1-2-3 Euler angles of the secondary in Fig. 29 in Appendix A. Again we see close agreement between the sphere-ellipsoid and GUBAS models. Note the secondary rolls over occasionally in the GUBAS model and θ_1 oscillates about 180° instead of 0° , but this is only a small deviation from the behavior seen in the sphere-ellipsoid model.

While there are quantitative differences between the sphere-ellipsoid and GUBAS models, they share qualitatively the same behavior. This is expected, as the high-fidelity model simply includes additional perturbations to the dynamics compared to the simple sphere-ellipsoid model. Most importantly, we are mainly concerned with the overall trends caused by dissipation, which are consistent across the models.

6. Short-Term Implications

More applicable to the AIDA collaboration is how much the Didymos system will evolve between the DART impact and the arrival of Hera to survey the system; this timespan is around 5 years. Thus, we next investigate how different secondary shapes cause different behaviors over this shorter timespan. Given the large number of systems we must test to cover possible secondary sizes, we return to the sphere-ellipsoid model for computational efficiency.

6.1. Secondary Energy

As seen in Fig. 6, the secondary energy does not initially evolve secularly but rather damps oscillations to approach a synchronous state. We can calculate the synchronous energy the secondary would have if it were in an equilibrium using the synchronous spin rate of the system calculated by Scheeres (2009):

$$\dot{\theta}^2 = \frac{\mathcal{G}(M_A + M_B)}{r^3} \left[1 + \frac{3}{2r^2} \left(\bar{I}_{B,z} + \bar{I}_{B,y} - 2\bar{I}_{B,x} \right) \right] \quad (34)$$

where the bodies are separated by a distance of r , and the bar indicates the mass-normalized secondary inertia values. Using this equilibrium spin rate, the secondary's minimum energy state at any time is simply calculated as:

$$E_{min} = \frac{1}{2} I_{B,z} \dot{\theta}^2. \quad (35)$$

Fig. 14 shows the secondary's rotational energy along with its instantaneous synchronous energy over the first 5 years for the stable system ($a/b = 1.2$, $b/c = 1.1$).

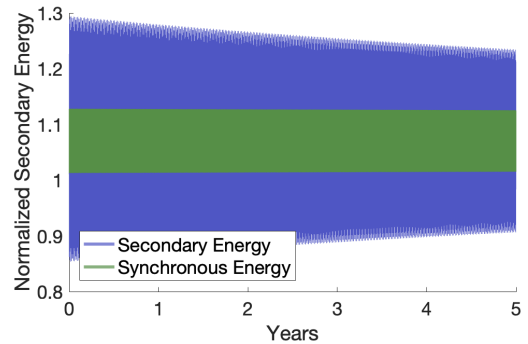


Figure 14: The secondary rotational energy for the stable system ($a/b = 1.2$, $b/c = 1.1$) in blue, along with the synchronous energy in green. The energy is normalized by the pre-impact equilibrium energy. The instantaneous energy approaches the synchronous value as energy dissipates.

We see the secondary energy approaching the synchronous state as the system dissipates energy. To quantify this we define the secondary excess energy, which is simply

$$E_{exc} = |E_B - E_{min}|. \quad (36)$$

By calculating changes in the excess energy, we can determine how close the system has moved to the synchronous

configuration. We investigate the secondary's energy change for all shapes by plotting the relative change in excess energy over 5 years in Fig. 15. The relative change is calculated as

$$\Delta E = \frac{\bar{E}_5 - \bar{E}_1}{\bar{E}_1} \quad (37)$$

where \bar{E}_5 is the mean excess energy over the fifth year of the simulation, and likewise for \bar{E}_1 . In other words, the relative change is the difference in the mean excess energy over the first and fifth (final) year of the simulation, normalized by the average excess energy during the first year. In Fig. 15, we see essentially random changes in the secondary excess energy for shapes within the unstable region (refer to Fig. 1 for an illustration of the unstable region, but generally this is in the region of high values of a/b and b/c). Due to the chaotic dynamics of these shapes, the secondary could actually be moving away from the synchronous state. Outside the unstable region, generally we see shapes with a small value of a/b have the largest relative change in excess energy, while secondaries with $a/b \approx 1.4$ have the smallest relative change. Interestingly, there is a large resonance in the system when $a/b \approx 1.4$ (Agrusa et al., 2021), which leads to a more energetic response in the secondary (higher initial libration amplitude; see Fig. 17 below), so the relative change in secondary energy is smaller.

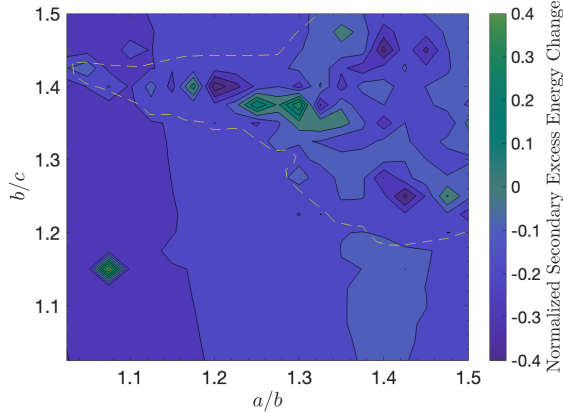


Figure 15: The normalized change in secondary excess energy after 5 years, calculated as the difference between the average secondary excess energy during the first and last year of the simulation, normalized by the average excess energy during the first year of the simulation. The yellow dashed line shows the approximate unstable region.

6.2. Free Energy

We next turn to the free energy, which is the sum of the secondary and orbit energies. By excluding the primary's energy, this allows us to better understand the system's evolution. We keep the same definition for the relative change in energy, but now applied to the free energy. The relative change in free energy is plotted in Fig. 16, where we see in general very small changes in the first 5 years. However, as discussed above, in some systems the free energy is initially decreasing. In Fig. 16 we see this is the case for most

systems, as only shapes with a small value of a/b immediately start increasing free energy. We point out that as the orbit expands (semimajor axis increases), we would expect the free energy to also increase as the orbit energy increases, yet this is not the case during the first years after the perturbation. This once again highlights the departure from classical tidal theory during the initial period of libration damping as dissipation pushes the system back toward an equilibrium. Again we see the effect of the resonance at $a/b = 1.4$, as shapes near this area (and outside the unstable region) have the largest relative decrease in free energy over the first 5 years. Within the unstable region generally the free energy is decreasing, but this is not true for every shape, illustrating the chaotic nature of this region.

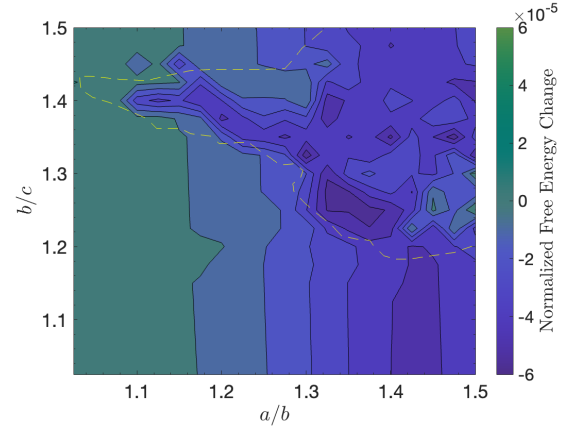


Figure 16: The percent change in free energy after 5 years, calculated as the difference between the average free energy during the first and last year of the simulation, normalized by the average energy during the first year of the simulation. The yellow dashed line shows the approximate unstable region.

6.3. Libration

Of particular interest is the libration amplitude of the system, as this will be a physically observable quantity with Hera. Here, we are defining libration as the angle between the secondary's long axis and the radial vector from the secondary to the primary. Thus, a system in equilibrium will have zero libration as the secondary's long axis is exactly aligned with the primary. In Fig. 17, we plot the initial libration amplitude after the impact. Generally, we see the libration amplitude increases with the secondary's elongation, but begins to drop off after the resonance near $a/b = 1.4$, which is where the libration amplitude is at a maximum. Outside the unstable region, libration amplitude is essentially independent of b/c , but within the unstable region we generally see larger libration amplitudes as a result of the out-of-plane secondary rotation.

There is a correlation between the initial libration amplitude and the initial free energy trend, which can be seen when comparing Figs. 16 and 17. Generally, a larger libration amplitude corresponds to a faster decrease in free energy, while systems with a small libration amplitude immediately start increasing free energy. This indicates that

an initial decrease in free energy could be caused by a large perturbation away from equilibrium, as dissipation forces the system back toward an equilibrium configuration.

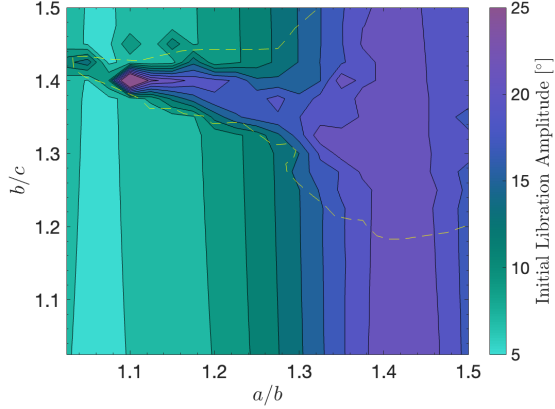


Figure 17: The initial libration amplitude at the start of the simulation. The yellow dashed line shows the approximate unstable region, which generally has the largest libration amplitudes.

Fig. 18 plots the change in libration amplitude after 5 years. This is calculated by finding the difference between the maximum libration angles between the first and last year of the simulation. Within the unstable region, the system can increase or decrease the libration amplitude over this short time span depending on the shape. Thus, if the DART impact causes Dimorphos to become attitude unstable, Hera won't observe any systematic trend in libration amplitude and instead see chaotic variations due to the non-principal axis rotation. However, outside the unstable region there is a systematic decrease in libration amplitude, although only a few degrees for our selected values of Q/k . However, the largest decrease in libration amplitude outside the chaotic region is around $a/b = 1.1$, which is another resonance (Agrusa et al., 2021). These systems could see a decrease in libration amplitude of around 3-4°, which is noteworthy considering these same systems have a small initial libration amplitude of around 8-10°. Thus, it's possible Dimorphos could dissipate a significant fraction of the DART-induced libration amplitude by the time of Hera's arrival, of course depending on the true tidal parameters of the system. A discussion of the effect of Q/k on libration damping is included in Section 8.

6.4. Eccentricity

Next we examine the Keplerian eccentricity of the system. Fig. 19 plots the maximum eccentricity over the first year after the perturbation, where we see shapes with large values of a/b and b/c have the largest initial eccentricity. There appears to be no effect from the unstable region on the initial eccentricity. However, this is not the case for the change in eccentricity over 5 years, shown in Fig. 20. Here we see the largest decreases in eccentricity are found for shapes in the unstable region, consistent with the findings of

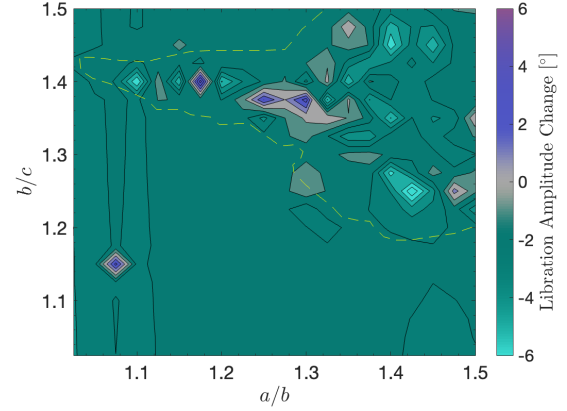


Figure 18: The change in libration amplitude after 5 years, calculated as the difference between the maximum libration during the first and last year of the simulation. The yellow dashed line shows the approximate unstable region, in which the libration amplitude can change randomly.

Quillen et al. (2020). Outside the unstable region, as a/b increases so does the change in eccentricity. Thus, it appears the shapes with the largest initial libration amplitudes also see the largest decrease in eccentricity during the first years after the perturbation. These are also the same shapes with the largest initial decrease in free energy, but the smallest relative change in secondary excess energy. This highlights the importance of spin-orbit coupling, as systems pushed furthest away from equilibrium see the fastest changes to their orbit in order to bring the secondary's spin back to an equilibrium.

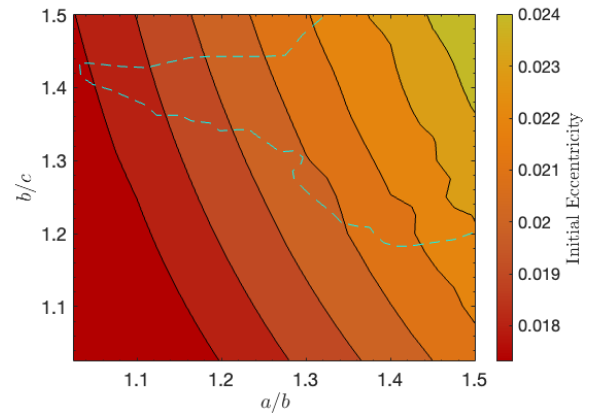


Figure 19: The initial eccentricity, calculated as the maximum eccentricity during the first year of the simulation. The cyan dashed line shows the approximate unstable region, which has no bearing on the initial eccentricity.

7. BYORP

While this analysis has focused on the internal system dynamics of a binary asteroid, an important external influence on the dynamics is BYORP (Ćuk and Burns, 2005).

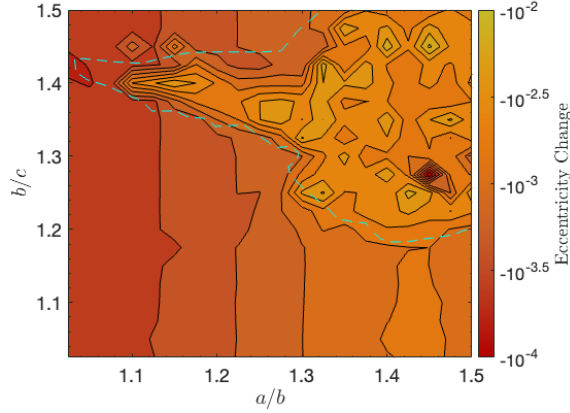


Figure 20: The change in eccentricity after 5 years, calculated as the difference between the maximum eccentricity during the first and last year of the simulation. The results are plotted on a logarithmic scale for clarity. The cyan dashed line shows the approximate unstable region, which sees the largest change in eccentricity.

For a singly synchronous binary system, BYORP can act to either expand or contract the orbit, with NPA rotation decreasing the magnitude of the BYORP torque (Quillen et al., 2022). Thus, we expect the BYORP effect to have a smaller impact on the dynamics of the unstable systems where NPA rotation is frequent.

Jacobson and Scheeres (2011b) predict an equilibrium in which tidal dissipation balances BYORP drift, and the orbit does not evolve over time. Didymos has a very small mean anomaly drift rate of $\Delta M = 0.15 \pm 0.14^\circ \text{yr}^{-2}$ with 3σ uncertainty (Scheirich and Pravec, 2022), meaning that if it is not in a tide-BYORP equilibrium, it is likely near one. For our purposes we will assume an equilibrium between tides and BYORP in order to calculate a BYORP coefficient as a check on our analysis. Given the small observed mean anomaly drift, we can make this assumption without introducing too much error. In such an equilibrium, we can calculate:

$$\frac{BQ_A}{k_A} = \frac{2\pi\omega_d^2\rho R_A^2 q^{4/3}}{H_\odot a^7} \quad (38)$$

where $\omega_d = \sqrt{4\pi G\rho/3}$ is the spin disruption limit, $q = M_B/M_A$ is the mass ratio (under a uniform system bulk density assumption, this is equivalent to a volume ratio), R_A and a are the primary's mean radius and the binary mutual semimajor axis, respectively, and H_\odot is a solar parameter defined as

$$H_\odot = \frac{F_s}{a_\odot^2 \sqrt{1 - e_\odot^2}} \quad (39)$$

where $F_s \approx 1 \times 10^{17}$ is a constant and a_\odot , e_\odot are the heliocentric semimajor axis and eccentricity of Didymos, respectively (McMahon and Scheeres, 2010).

Likely, magnitudes of B exist in the interval from 0 to 10^{-2} , but most commonly values of B are reported between

10^{-3} and 10^{-2} (Scheirich et al., 2015; Jacobson and Scheeres, 2011b; Steinberg et al., 2011). With our parameters for Didymos and our value for Q_A/k_A , we calculate $B \approx 4.5 \times 10^{-3}$, which is within the expected interval.

Using Eq. 38, we can calculate the relationship between B and Q_A/k_A for our nominal Didymos system, shown in Fig. 21, for a BYORP-tide equilibrium. There is additional uncertainty around the size of both Didymos and Dimorphos, as well as the system bulk density which we have calculated independently using the system dynamics. Using the error bars on the size and density of these bodies, we also plot an uncertainty envelope around the BQ_A/k_A curve in Fig. 21.

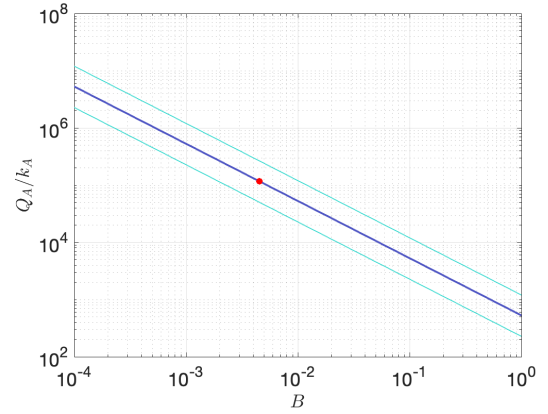


Figure 21: Q_A/k_A as a function of the BYORP coefficient B for our nominal Didymos system, plotted in dark blue. The uncertainty envelope around this curve is plotted in cyan considering the error bars in the bodies' estimates of sizes and densities. Our estimate is shown as a red dot on the plot.

On Fig. 21, we plot our nominal estimate for B that matches the Q_A/k_A value we adopted as a red dot. While this corresponds to a reasonable value of B , there is still a range of possibilities that should be considered. For example, for values of B within $10^{-3} - 10^{-2}$, Q_A/k_A could vary by nearly an order of magnitude in either direction. While the consistency seen here lends confidence to our selection of Q_A/k_A , we will investigate the role different values of Q/k have on energy dissipation, for both the primary and secondary.

In Didymos, BYORP acts to contract the orbit (decrease the semimajor axis) (Scheirich and Pravec, 2022). However, from our analysis, the time for eccentricity and libration to damp to nearly zero is relatively fast and the semimajor axis changes on the order of only 1 meter during this time (see Figs. 7 and 9). Thus, during the timescale we are interested in for this analysis, we expect BYORP to have very little effect on the dynamics, mainly decreasing the secular slope of semimajor axis evolution. Furthermore, Quillen et al. (2022) predict that the BYORP effect is weakened as a result of NPA rotation, so unstable systems would be affected even less.

The BYORP coefficient is primarily a function of Dimorphos' shape, thus the impact and subsequent reshaping of Di-

morphos will change the coefficient at some level. Previous work has shown that significant reshaping of Dimorphos is possible (Hirabayashi et al., 2022; Nakano et al., 2022; Raducan and Jutzi, 2022), so it is difficult to predict what level of change there will be in the BYORP coefficient. For a small change where BYORP remains contractive, Eq. 38 indicates that the shift in equilibrium will be small. However if B changes significantly, there could be a significant change to the equilibrium semimajor axis (if BYORP is contractive) or BYORP could act expansively along with tides to grow the orbit over time. In either case, however, even a significantly higher BYORP rate in either direction will have minimal effect on the orbit over the coming decades.

8. Effect of Tidal Parameters

As previously mentioned, there is considerable uncertainty surrounding the tidal parameters Q/k for both the primary and secondary. In Section 7 we saw Q_A/k_A can vary by an order of magnitude in either direction and still maintain consistency with a reasonable BYORP coefficient and the uncertainty around the shape and density of Didymos. Thus, we define three values for Q_A/k_A to test: 10^4 , 10^5 , and 10^6 . We use these same values to test Q_B/k_B as well. First, we vary Q_A/k_A over these three values while holding $Q_B/k_B = 10^5$ constant. Then we perform the opposite test by varying Q_B/k_B over the same values while holding Q_A/k_A constant. In this way we can determine which behaviors in the system rely mainly on the primary or secondary. Given how quickly dissipation occurs in our analysis in Section 4, we do not think it likely that Q/k is below 10^4 , and even if it is this would only speed up the process already observed. Furthermore, it is possible that Q/k is larger than 10^6 , but if this is the case, again the system would only evolve more slowly than the 10^6 cases we test below. Thus, this range of Q/k values for both bodies gives us an idea on how the tidal parameter affects the system evolution. We perform this analysis for both the stable and unstable systems.

8.1. Stable System

For the stable system ($a/b = 1.2$, $b/c = 1.1$), we first hold $Q_B/k_B = 10^5$ constant and vary Q_A/k_A between 10^4 and 10^6 . In Fig. 22, we plot the libration amplitude, free energy, semimajor axis, and eccentricity over 200 years. The free energy has been normalized by its pre-impact equilibrium value. Note this is not a long enough time span for the system to fully equilibrate, but it is long enough to see the secular behavior of the system.

From Fig. 22, we see the dissipation of the libration amplitude has very little dependence on Q_A/k_A , indicating it depends almost solely on Q_B/k_B . Conversely, the semimajor axis has a strong dependence on Q_A/k_A , as evidenced in the plot of free energy and semimajor axis. These dependencies are expected from classical tidal theory. Unsurprisingly, smaller Q_A/k_A values (more dissipative systems) expand the orbit more rapidly than large values of Q_A/k_A . For

small Q_A/k_A values, the secular trend is faster than the dissipation in semimajor axis oscillations, whereas large Q_A/k_A values see the opposite, where oscillations in semimajor axis are damped faster than the secular trend becomes dominant. In the plot of free energy, we see the least dissipative system slowly losing free energy while the other systems are monotonically increasing, which is consistent with the behavior seen in the semimajor axis. Overall this indicates that when Q_A/k_A is larger than Q_B/k_B , the system contracts its orbit first to damp semimajor axis oscillations and libration amplitude, whereas when Q_A/k_A is smaller than Q_B/k_B , the orbit expands faster than the secondary re-equilibrates. Lastly, the eccentricity damping also appears to have only a small dependence on Q_A/k_A , as there are only small differences in the trend between the values tested here.

Next, we perform the complement of this analysis by holding $Q_A/k_A = 10^5$ constant and varying Q_B/k_B between 10^4 and 10^6 . In Fig. 23, we plot the libration amplitude, the free energy, semimajor axis, and eccentricity over 200 years.

In Fig. 23, we see the dissipation of the libration amplitude has a strong dependence on Q_B/k_B , with smaller values (more dissipative) damping libration faster. Looking at the free energy, the secular trend appears to have only a small dependence on Q_B/k_B , but for small values of Q_B/k_B we see the initial decrease in free energy. While the case $Q_B/k_B = Q_A/k_A = 10^5$ appears to have a slope different from the other cases, its slope is actually changing slowly and approaching the same rate as the others. The free energy corresponds to the semimajor axis, where the secular trend again sees only a small dependence on Q_B/k_B , but the rate of damping oscillations does have a strong dependence on Q_B/k_B . The most dissipative system ($Q_B/k_B = 10^4$) damps the oscillations fastest and appears to have an initial trend of decreasing semimajor axis (consistent with the decrease in free energy). This indicates that systems with a very dissipative secondary initially contract the orbit to reestablish equilibrium. Lastly, we see a strong dependence of eccentricity damping on Q_B/k_B , with more dissipative systems unsurprisingly damping eccentricity the fastest. Again, these dependencies are expected from classical tidal theory.

8.2. Unstable System

We next repeat the same analysis by varying Q_A/k_A and Q_B/k_B for the unstable system ($a/b = 1.4$, $b/c = 1.3$). First, we hold $Q_B/k_B = 10^5$ constant while varying Q_A/k_A between 10^4 and 10^6 . We plot the libration amplitude, free energy, semimajor axis, and eccentricity for this analysis in Fig. 24.

Overall, we see very similar behavior between the unstable and stable system. Consistent with classical tidal theory, it appears the libration amplitude and eccentricity damping are largely unaffected by the value of Q_A/k_A during this time. Again, the secular trend of free energy and semimajor axis strongly depend on Q_A/k_A as expected. When $Q_A/k_A > Q_B/k_B$ (i.e. $Q_A/k_A = 10^6$, $Q_B/k_B = 10^5$), the damping rate of semimajor axis oscillations is faster than the

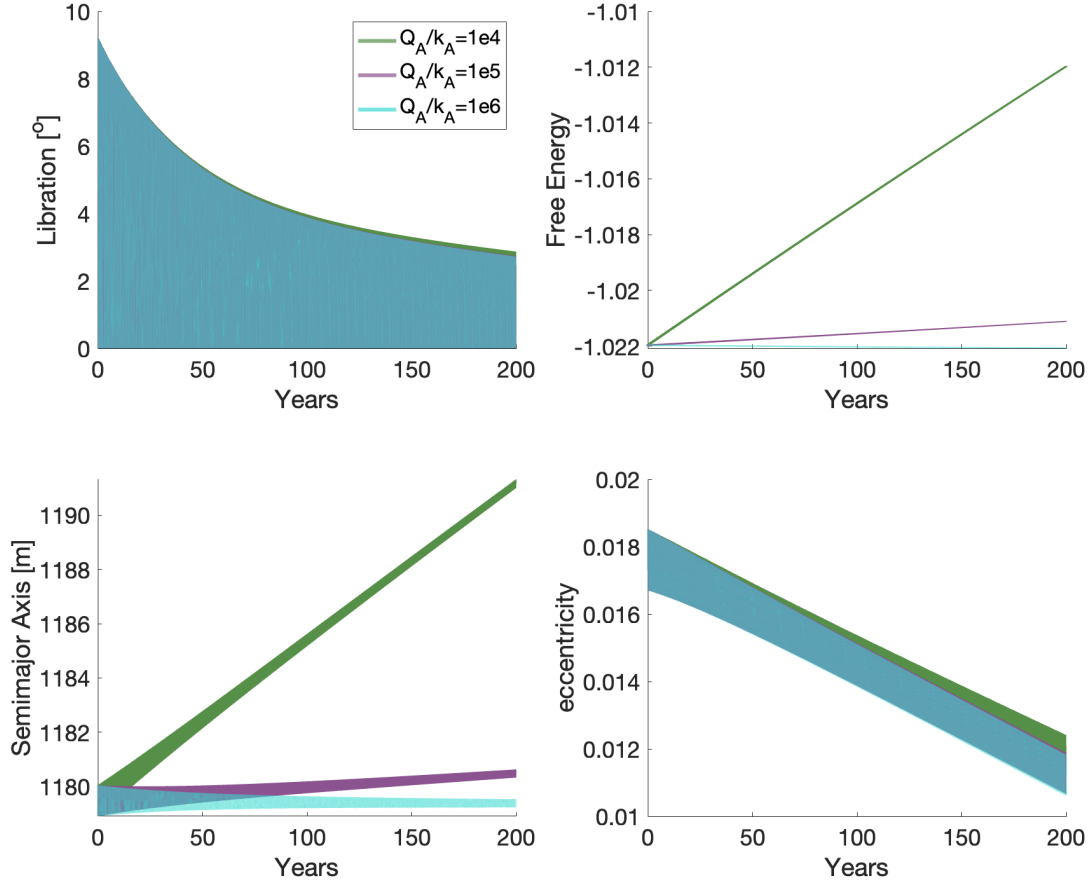


Figure 22: For the stable system $a/b = 1.2$, $b/c = 1.1$, we vary the value of Q_A/k_A while keeping $Q_B/k_B = 10^5$ constant. For 200 years, we plot the libration angle (top left), normalized free energy (top right), semimajor axis (bottom left), and eccentricity (bottom right). While the rate of change of the semimajor axis and free energy strongly depend on Q_A/k_A , the libration amplitude and eccentricity are largely independent of primary tidal parameters.

secular trend, and as a result we see an overall decrease in the free energy. At a longer timescale we expect both the semimajor axis and free energy to begin increasing as the orbit expands.

We next hold $Q_A/k_A = 10^5$ constant and vary Q_B/k_B between 10^4 and 10^6 . For this test, the libration amplitude, free energy, semimajor axis, and eccentricity are plotted in Fig. 25.

Again, there are strong similarities between the unstable and stable case. The damping rate of libration amplitude and eccentricity strongly depend on Q_B/k_B , while the secular trends in semimajor axis and free energy seem ignorant of Q_B/k_B , as expected from classical tidal theory. However, the damping rate of semimajor axis oscillations does depend heavily on Q_B/k_B , with more dissipative secondaries (small Q_B/k_B) damp these oscillations faster than the secular trend develops, and as a result the free energy of the system initially decreases.

Based on these analyses of Q_A/k_A and Q_B/k_B , we can conclude that the libration amplitude, eccentricity, and oscillations in semimajor axis mostly depend on Q_B/k_B , while the secular trend of the orbit, i.e. semimajor axis expansion, is driven by Q_A/k_A . When systems have a more dissipative secondary, they re-enter equilibrium before any noticeable secular change in the orbit develops, whereas when systems have a more dissipative primary the re-equilibration of the secondary takes longer than the secular evolution of the orbit.

9. Discussion

In this work we attempt to outline the possibilities of energy dissipation after a DART-like perturbation both in the long- and near-term, investigating dissipation both in stable and tumbling systems. We implement tidal torque and non-principal axis dissipation in a simple sphere-ellipsoid approximation of binary asteroids. We find that both sta-

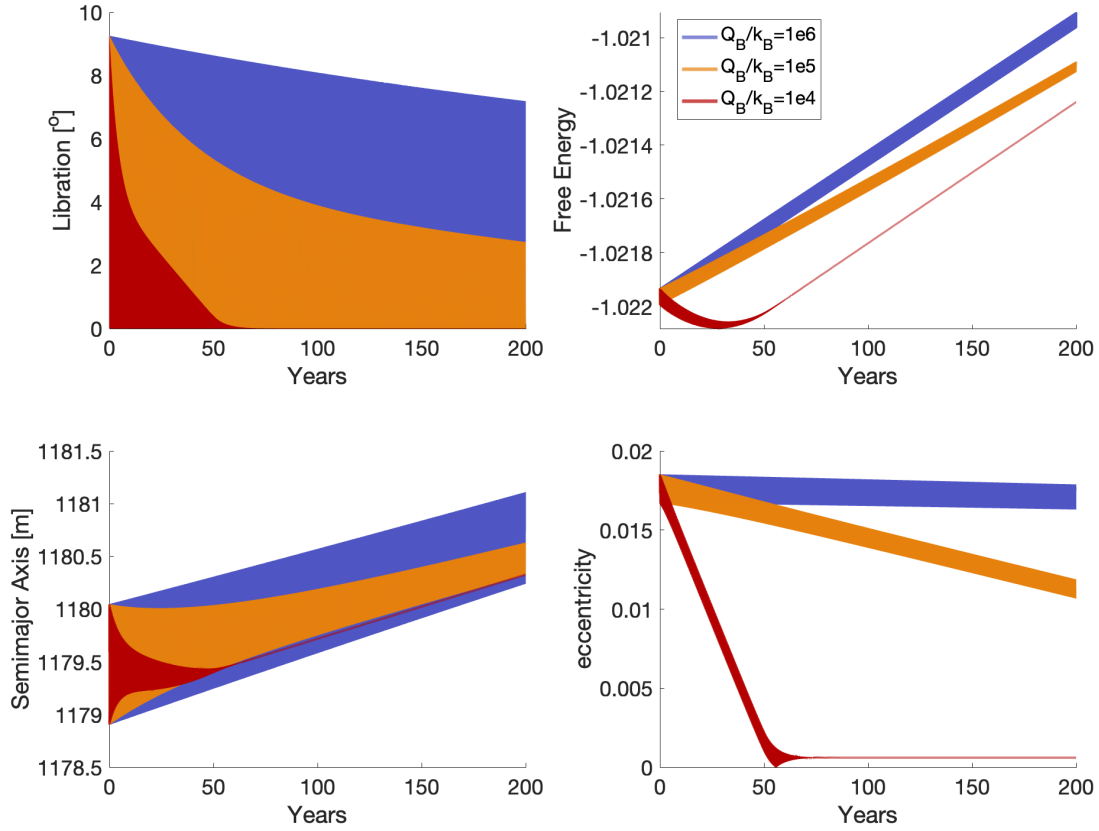


Figure 23: For the stable system $a/b = 1.2$, $b/c = 1.1$, we vary the value of Q_B/k_B while keeping $Q_A/k_A = 10^5$ constant. For 200 years, we plot the libration angle (top left), normalized free energy (top right), semimajor axis (bottom left), and eccentricity (bottom right). The dissipation rates of the libration amplitude and eccentricity strongly depend on Q_B/k_B . For very dissipative secondaries, the free energy initially decreases, which is not the case for secondaries with larger Q_B/k_B values. The secular rate of semimajor axis expansion seems independent of Q_B/k_B , but the damping rate of oscillations in semimajor axis does depend on Q_B/k_B .

ble and tumbling systems dissipate energy on comparable timescales to return to a synchronous configuration. Previous studies have claimed that tumbling greatly reduces the rate of energy dissipation (Wisdom et al., 1984; Naidu and Margot, 2015; Quillen et al., 2022), but this is only for the non-synchronous case. Our results agree with Quillen et al. (2020) in that tumbling within the synchronous state can increase energy dissipation, and the libration amplitude damps to zero before predicted for planar rotation. A unique result we find is that non-principal axis rotation can damp as quickly as planar libration for strongly coupled systems with efficient dissipation. We find in these systems the libration amplitude, both stable and unstable, is tied closely to the orbit eccentricity and oscillations in the semimajor axis, as all of these dissipate on the same timescale. For especially dissipative systems, the system returns to equilibrium before any substantial secular trend is apparent.

For near-term dynamics relevant to the Hera mission, we

find systems experiencing stable in-plane libration systematically dissipate energy to return to an equilibrium, synchronous configuration. However, systems with out-of-plane tumbling do not have a systematic trend during the short time between DART's impact and Hera's rendezvous thanks to chaotic dynamics. Thus, the shape of Dimorphos is paramount in predicting energy dissipation, as not only does the shape place the system in the stable/unstable region, it also dictates the magnitude of post-impact libration. Generally, more elongated shapes and shapes in the unstable region have the largest libration amplitude and the largest relative change in free energy following the impact. However, the secondary excess energy can vary randomly within the unstable region, and in the stable region less elongated shapes (i.e. shapes with a smaller initial libration amplitude) have the largest relative decrease in secondary excess energy. The rate of libration damping also depends on the shape, as unstable shapes again can see random changes in the libration amplitude. In the

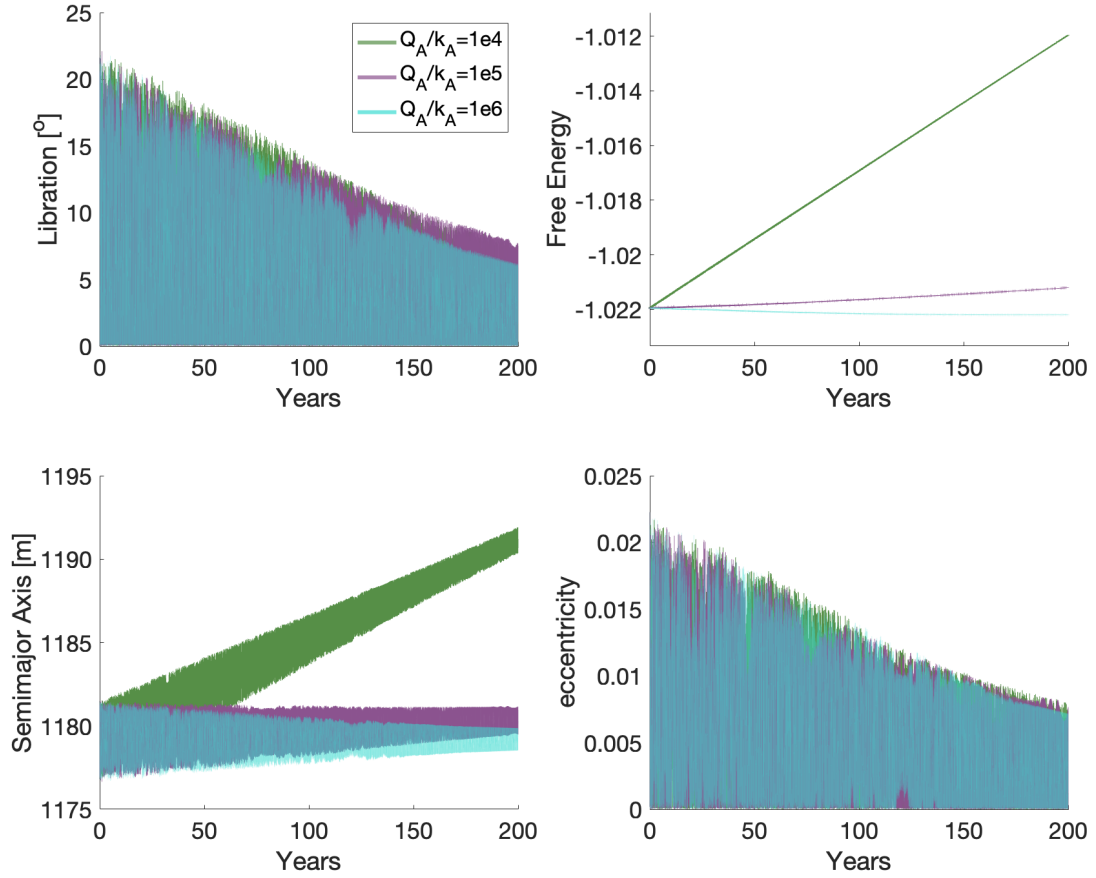


Figure 24: For the unstable system $a/b = 1.4$, $b/c = 1.3$, we vary the value of Q_A/k_A while keeping $Q_B/k_B = 1 \times 10^5$ constant. For 200 years, we plot the libration angle (top left), normalized free energy (top right), semimajor axis (bottom left), and eccentricity (bottom right). While the rate of change of the semimajor axis and free energy strongly depend on Q_A/k_A , the libration amplitude and eccentricity are largely independent of primary tidal parameters.

stable region, resonances play a large role in how the libration amplitude dissipates, but in general this is not expected to exceed a few degrees in the years between the DART impact and Hera's arrival, even in the most dissipative cases. However, there are some cases, with a very dissipative secondary, in which a small initial libration amplitude can decrease by 20-30%. The largest decrease in eccentricity is found for shapes with the largest initial libration amplitude, but overall this change is still small, on the order of 0.01 over 5 years for very dissipative systems. Thus, there is potential for non-negligible changes to occur in the system before Hera's arrival, contingent on the secondary's stiffness.

While BYORP will factor in to the evolution of the system, we believe it will have a negligible effect on the actual libration damping. In Didymos, BYORP contracts the orbit, or shrinks the semimajor axis (Scheirich and Pravec, 2022). Given the small mean anomaly drift rate, Didymos is likely near a tide-BYORP equilibrium in which the tidal expansion

is nearly balanced by the BYORP effect. As a result, we can make a prediction of the BYORP coefficient, which is consistent with expected values. After the impact, the system will dissipate energy to reduce libration and eccentricity, while damping oscillations in the semimajor axis. During this time, BYORP will continue to shrink the semimajor axis, unless the impact causes significant reshaping of the secondary and changes the BYORP coefficient. However, the secular rate of semimajor axis change is already small, and generally independent of the oscillations (the secular rate is driven by the primary, whereas the oscillations are driven by the secondary). Furthermore, NPA rotation will also decrease the BYORP effect (Quillen et al., 2022). Thus, we predict the process of libration damping will be largely independent of the secular changes caused by BYORP over the timeframe of interest here.

By varying Q/k for both the primary and secondary, we find that the rate of libration and eccentricity damping are

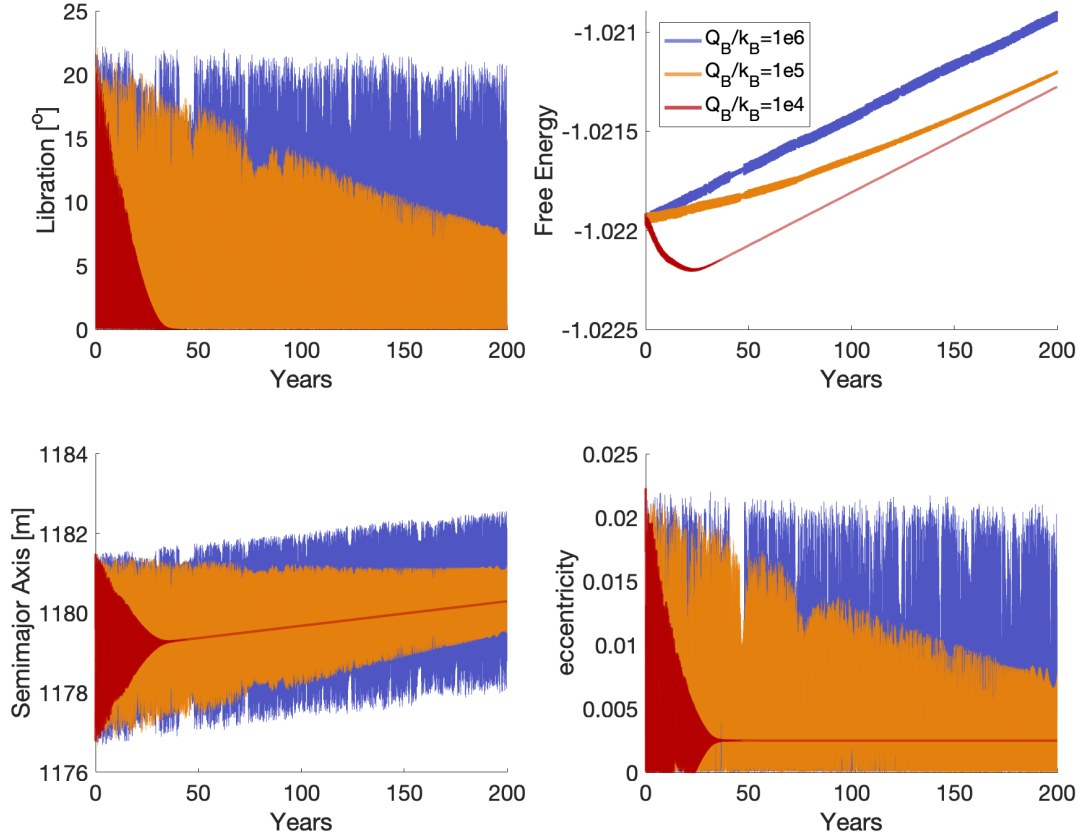


Figure 25: For the unstable system $a/b = 1.4$, $b/c = 1.3$, we vary the value of Q_B/k_B while keeping $Q_A/k_A = 1 \times 10^5$ constant. For 200 years, we plot the libration angle (top left), normalized free energy (top right), semimajor axis (bottom left), and eccentricity (bottom right). The dissipation rates of the libration amplitude and eccentricity strongly depend on Q_B/k_B . For very dissipative secondaries, the free energy initially decreases, which is not the case for secondaries with larger Q_B/k_B values. The secular rate of semimajor axis expansion seems independent of Q_B/k_B , but the damping rate of oscillations in semimajor axis does depend on Q_B/k_B .

strongly dependent on the secondary's tidal parameters, but largely independent of the primary's. By extension, the oscillations in the semimajor axis also are mainly dependent on the secondary's tidal parameters. Conversely, the secular trend in the semimajor axis mainly depends on the primary's tidal parameters, but not the secondary's. Thus, we find systems with $Q_B/k_B < Q_A/k_A$ damp libration and eccentricity faster than secular changes in the orbit become apparent. This also corresponds to an initial decrease in the free energy before the semimajor axis begins expanding, unless the initial libration amplitude is small. On the other hand, when $Q_B/k_B > Q_A/k_A$, the secular trend in the orbit is immediately obvious and the damping of libration and eccentricity is relatively slow in comparison. Thus, if the secondary is very dissipative, Hera may be able to measure the damping of the libration amplitude and eccentricity. In these very dissipative systems, the coupling between eccentricity and libration means the eccentricity dissipates much faster than predicted

by the analytic models of Goldreich and Sari (2009). Consequently, we do not recommend using an analytic model to approximate evolution of a coupled system experiencing libration, unless this system is not very dissipative or is already in an equilibrium. This also suggests close binary asteroids with measured eccentricity have either a tumbling secondary or a stiff, non-dissipative secondary, consistent with Pravec et al. (2016).

Future work on this topic is necessary after both the DART impact and Hera's survey. These missions will provide more information on the system, specifically the secondary shape and impact strength from DART and LICIAcube and the density and constraints on the tidal parameters from Hera. With estimates on these parameters, more accurate predictions can be made on the energy dissipation from Didymos.

Acknowledgements

The authors would like to acknowledge the DART investigation team for helpful discussion throughout this study's development and preparation. We also thank Dr. Federico Zoppetti for several useful conversations regarding the intricacies of tidal torque models. This study was supported in part by the DART mission, NASA contract No. 80MSFC20D0004 to JHU/APL. A.J.M. acknowledges support from the Planetary Defense Conference student grant. G.N. and Ö.K. acknowledge support by Belgian Federal Science Policy (BELSPO) through the ESA/PRODEX Program. R.N. acknowledges support from NASA/FINESST (NNH20ZDA001N/80NSSC2

The simulations shown in Fig. 1 were carried out on The University of Maryland Astronomy Department's YORP cluster, administered by the Center for Theory and Computation.

A. Supplementary Figures

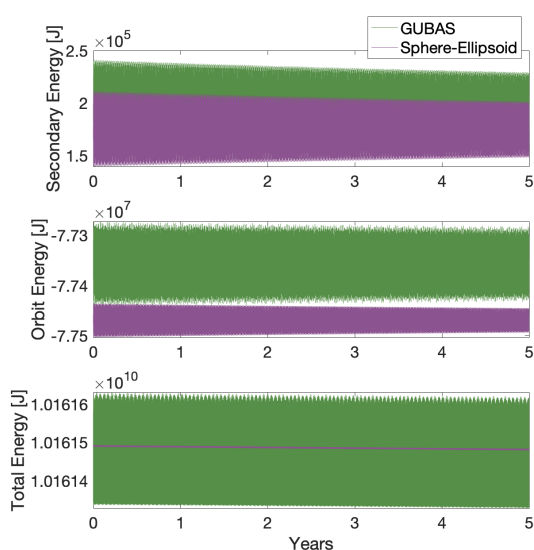


Figure 26: The secondary energy (top), orbit energy (middle), and total energy (bottom) of the stable system ($a/b = 1.2$, $b/c = 1.1$) for the sphere-ellipsoid and high-fidelity GUBAS models. While there are differences between the models, the overall trends are consistent.

References

- Agrusa, H., Ballouz, R., Meyer, A.J., Tasev, E., Noiset, G., Karatekin, Ö., Michel, P., Richardson, D.C., Hirabayashi, M., 2022. Rotation-induced granular motion on the secondary component of binary asteroids: Application to the dart impact on dimorphos. *Astronomy & Astrophysics* 664, L3. doi:<https://doi.org/10.1051/0004-6361/202244388>.
- Agrusa, H.F., Ferrari, F., Zhang, Y., Richardson, D.C., Michel, P., 2022. Dynamical evolution of the didymos- dimorphos binary asteroid as rubble piles following the dart impact. *The Planetary Science Journal* 3, 158. doi:<https://doi.org/10.3847/PSJ/ac76c1>.
- Agrusa, H.F., Gkolias, I., Tsiganis, K., Richardson, D.C., Meyer, A.J., Scheeres, D.J., Čuk, M., Jacobson, S.A., Michel, P., Karatekin, Ö., et al., 2021. The excited spin state of dimorphos resulting from the dart impact. *Icarus* 370, 114624.

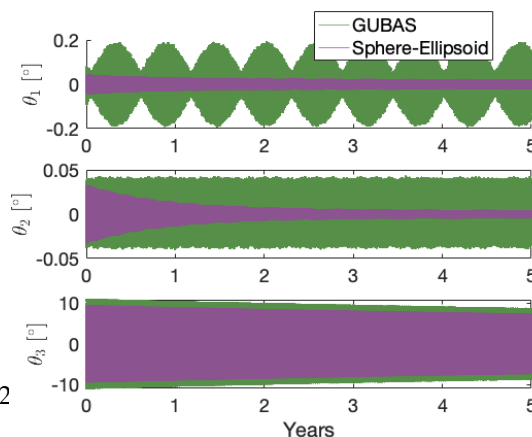


Figure 27: The 1-2-3 Euler angles of the stable system ($a/b = 1.2$, $b/c = 1.1$) for the sphere-ellipsoid and high-fidelity GUBAS models. While there are differences between the models, the overall trend is consistent.

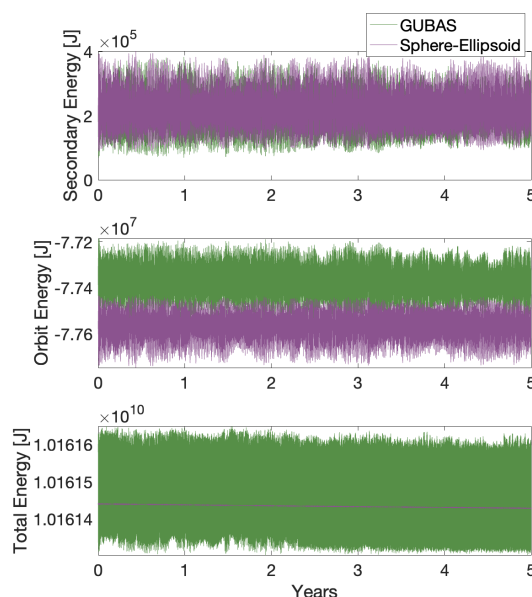


Figure 28: The secondary energy (top), orbit energy (middle), and total energy (bottom) of the unstable system ($a/b = 1.4$, $b/c = 1.3$) for the sphere-ellipsoid and high-fidelity GUBAS models. While there are differences between the models, the overall trends are consistent.

- Agrusa, H.F., Richardson, D.C., Davis, A.B., Fahnestock, E., Hirabayashi, M., Chabot, N.L., Cheng, A.F., Rivkin, A.S., Michel, P., Group, D.D.W., et al., 2020. A benchmarking and sensitivity study of the full two-body gravitational dynamics of the dart mission target, binary asteroid 65803 didymos. *Icarus* 349, 113849. doi:<https://doi.org/10.1016/j.icarus.2020.113849>.
- Brack, D.N., McMahon, J.W., 2019. Modeling the coupled dynamics of an asteroid with surface boulder motion. *Icarus* 333, 96–112. doi:<https://doi.org/10.1016/j.icarus.2019.05.038>.
- Brasser, R., 2020. Efficient tidal dissipation in deimos. *Icarus* 347, 113791. doi:<https://doi.org/10.1016/j.icarus.2020.113791>.
- Breiter, S., Rožek, A., Vokrouhlický, D., 2012. Stress field and spin axis relaxation for inelastic triaxial ellipsoids. *Monthly Notices of the Royal Astronomical Society* 427, 755–769. doi:<https://doi.org/10.1111/j>.

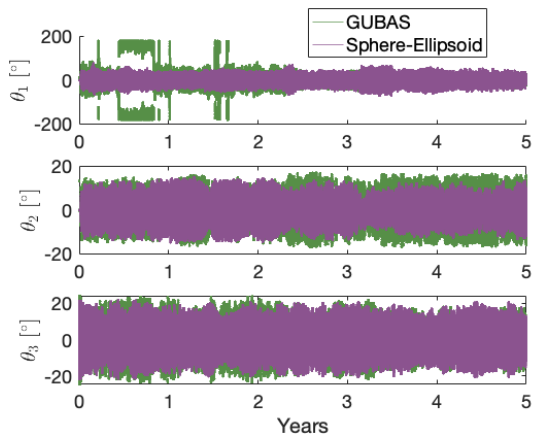


Figure 29: The 1-2-3 Euler Angles of the unstable system ($a/b = 1.4$, $b/c = 1.3$) for the sphere-ellipsoid and high-fidelity GUBAS models. While there are differences between the models, the overall trends are consistent.

- 1365–2966.2012.21970.x.
- Burns, J.A., Safronov, V., Gold, T., 1973. Asteroid nutation angles. *Monthly Notices of the Royal Astronomical Society* 165, 403–411. doi:<https://doi.org/10.1093/mnras/165.4.403>.
- Cheng, A.F., Rivkin, A.S., Michel, P., Atchison, J., Barnouin, O., Benner, L., Chabot, N.L., Ernst, C., Fahnestock, E.G., Kueppers, M., et al., 2018. Aida dart asteroid deflection test: Planetary defense and science objectives. *Planetary and Space Science* 157, 104–115. doi:<https://doi.org/10.1016/j.pss.2018.02.015>.
- Ćuk, M., Burns, J.A., 2005. Effects of thermal radiation on the dynamics of binary neas. *Icarus* 176, 418–431. doi:<https://doi.org/10.1016/j.icarus.2005.02.001>.
- Davis, A.B., Scheeres, D.J., 2020. Doubly synchronous binary asteroid mass parameter observability. *Icarus* 341, 113439. doi:<https://doi.org/10.1016/j.icarus.2019.113439>.
- Davis, A.B., Scheeres, D.J., 2021. Gubas: General use binary asteroid simulator. *Astrophysics Source Code Library*, ascl:2107.013.
- Efroimsky, M., 2015. Tidal evolution of asteroidal binaries, ruled by viscosity, ignorant of rigidity. *The Astronomical Journal* 150, 98. doi:<https://doi.org/10.1088/0004-6256/150/4/98>.
- Efroimsky, M., 2018. Dissipation in a tidally perturbed body librating in longitude. *Icarus* 306, 328–354. doi:<https://doi.org/10.1016/j.icarus.2017.10.020>.
- Ershkov, S.V., Leshchenko, D., 2019. On the dynamics of non-rigid asteroid rotation. *Acta Astronautica* 161, 40–43. doi:<https://doi.org/10.1016/j.actaastro.2019.05.011>.
- Feldhacker, J.D., Syal, M.B., Jones, B.A., Doostan, A., McMahon, J., Scheeres, D.J., 2017. Shape dependence of the kinetic deflection of asteroids. *Journal of Guidance, Control, and Dynamics* 40, 2417–2431. doi:<https://doi.org/10.2514/1.G002270>.
- Ferraz-Mello, S., 2013. Tidal synchronization of close-in satellites and exoplanets, a rheophysical approach. *Celestial Mechanics and Dynamical Astronomy* 116, 109–140. doi:<https://doi.org/10.1007/s10569-013-9482-y>.
- Goldreich, P., Sari, R., 2009. Tidal evolution of rubble piles. *The Astrophysical Journal* 691, 54. doi:<https://doi.org/10.1088/0004-637X/691/1/54>.
- Harris, A.W., Fahnestock, E.G., Pravec, P., 2009. On the shapes and spins of “rubble pile” asteroids. *Icarus* 199, 310–318. doi:<https://doi.org/10.1016/j.icarus.2008.09.012>.
- Hirabayashi, M., 2022. Dynamics of a deforming planetary body. *Icarus Accepted*.
- Hirabayashi, M., Ferrari, F., Jutzi, M., Nakano, R., Raducan, S.D., Sánchez, P., Soldini, S., Zhang, Y., Barnouin, O.S., Richardson, D.C., et al., 2022. Double asteroid redirection test (dart): Structural and dynamic interac-

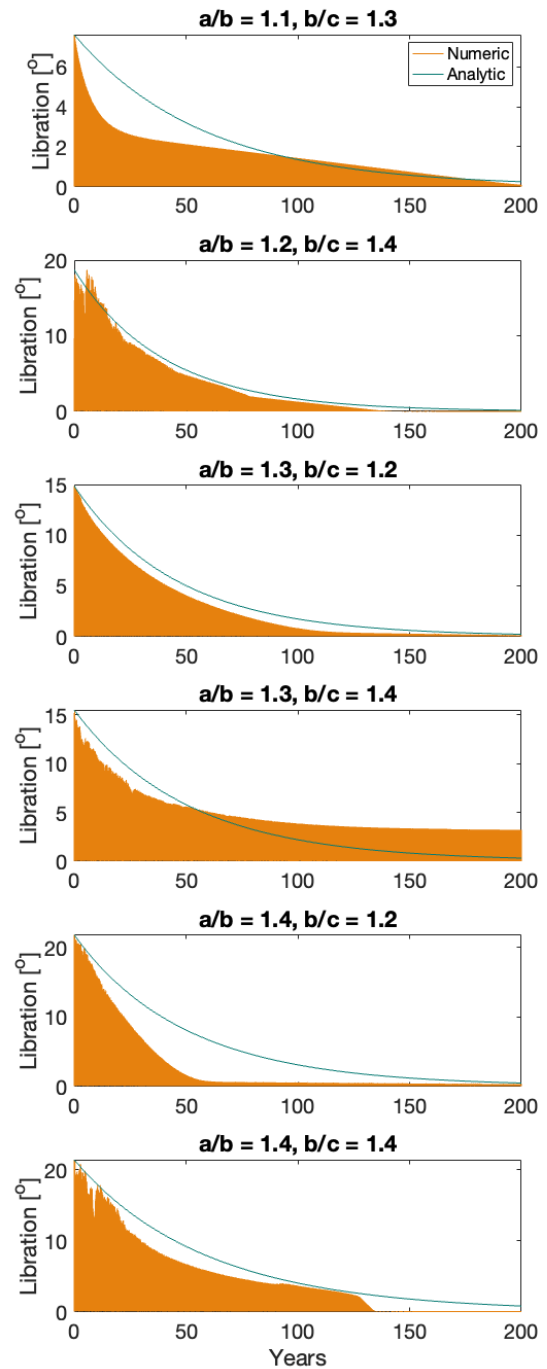


Figure 30: The libration amplitude for 6 additional secondary shapes from both the stable and unstable regions. Every shape has a similar damping timescale regardless of stability.

- tions between asteroidal elements of binary asteroid (65803) didymos. *The Planetary Science Journal* 3, 140. doi:<https://doi.org/10.3847/PSJ/ac6eff>.
- Hut, P., 1981. Tidal evolution in close binary systems. *Astronomy and Astrophysics* 99, 126–140.
- Jacobson, S.A., Scheeres, D.J., 2011a. Dynamics of rotationally fissioned asteroids: Source of observed small asteroid systems. *Icarus* 214, 161–178. doi:<https://doi.org/10.1016/j.icarus.2011.04.009>.
- Jacobson, S.A., Scheeres, D.J., 2011b. Long-term stable equilibria for synchronous binary asteroids. *The Astrophysical Journal Letters* 736, L19. doi:<https://doi.org/10.1088/2041-8205/736/1/L19>.
- Jacobson, S.A., Scheeres, D.J., McMahon, J., 2014. Formation of the wide asynchronous binary asteroid population. *The Astrophysical Journal* 780, 60. doi:<https://doi.org/10.1088/0004-637X/780/1/60>.
- Maciejewski, A.J., 1995. Reduction, relative equilibria and potential in the two rigid bodies problem. *Celestial Mechanics and Dynamical Astronomy* 63, 1–28. doi:<https://doi.org/10.1007/BF00691912>.
- McMahon, J., Scheeres, D., 2010. Detailed prediction for the byorp effect on binary near-earth asteroid (66391) 1999 kw4 and implications for the binary population. *Icarus* 209, 494–509. doi:<https://doi.org/10.1016/j.icarus.2010.05.016>.
- Meyer, A.J., Gkolias, I., Gaitanas, M., Agrusa, H.F., Scheeres, D.J., Tsiganis, K., Pravec, P., Benner, L.A., Ferrari, F., Michel, P., 2021. Libration-induced orbit period variations following the dart impact. *The planetary science journal* 2, 242. doi:<https://doi.org/10.3847/PSJ/ac3bd1>.
- Michel, P., Küppers, M., Bagatin, A.C., Carry, B., Charnoz, S., De Leon, J., Fitzsimmons, A., Gordo, P., Green, S.F., Hérique, A., et al., 2022. The esa hera mission: Detailed characterization of the dart impact outcome and of the binary asteroid (65803) didymos. *The Planetary Science Journal* 3, 160. doi:<https://doi.org/10.3847/PSJ/ac6f52>.
- Mignard, F., 1979. The evolution of the lunar orbit revisited. i. The Moon and the planets 20, 301–315. doi:<https://doi.org/10.1007/BF00907581>.
- Molina, A., Moreno, F., Martínez-López, F., 2003. Energy dissipation by internal stresses in a free-rotating symmetric ellipsoid: Application to comet p/halley. *Astronomy & Astrophysics* 398, 809–817. doi:<https://doi.org/10.1051/0004-6361:20021742>.
- Murray, C.D., Dermott, S.F., 1999. *Solar system dynamics*. Cambridge university press.
- Naidu, S., Benner, L., Brozovic, M., Nolan, M., Ostro, S., Margot, J., Giorgini, J., Hirabayashi, T., Scheeres, D., Pravec, P., et al., 2020. Radar observations and a physical model of binary near-earth asteroid 65803 didymos, target of the dart mission. *Icarus* 348, 113777. doi:<https://doi.org/10.1016/j.icarus.2020.113777>.
- Naidu, S.P., Margot, J.L., 2015. Near-earth asteroid satellite spins under spin-orbit coupling. *The Astronomical Journal* 149, 80. doi:<https://doi.org/10.1088/0004-6256/149/2/80>.
- Nakano, R., Hirabayashi, M., Agrusa, H.F., Ferrari, F., Meyer, A.J., Michel, P., Raducan, S.D., Sánchez, P., Zhang, Y., 2022. Nasa's double asteroid redirection test (dart): Mutual orbital period change due to reshaping in the near-earth binary asteroid system (65803) didymos. *The Planetary Science Journal* 3, 148. doi:<https://doi.org/10.3847/PSJ/ac7566>.
- Nimmo, F., Matsuyama, I., 2019. Tidal dissipation in rubble-pile asteroids. *Icarus* 321, 715–721. doi:<https://doi.org/10.1016/j.icarus.2018.12.012>.
- Pravec, P., Harris, A.W., Scheirich, P., Kušnirák, P., Šarounová, L., Hergenrother, C.W., Mottola, S., Hicks, M., Masi, G., Krugly, Y.N., et al., 2005. Tumbling asteroids. *Icarus* 173, 108–131. doi:<https://doi.org/10.1016/j.icarus.2004.07.021>.
- Pravec, P., Scheirich, P., Kušnirák, P., Hornoch, K., Galád, A., Naidu, S., Pray, D., Világi, J., Gajdoš, Š., Kornoš, L., et al., 2016. Binary asteroid population. 3. secondary rotations and elongations. *Icarus* 267, 267–295. doi:<https://doi.org/10.1016/j.icarus.2015.12.019>.
- Pravec, P., Thomas, C., Rivkin, A., Scheirich, P., Moskovitz, N., Knight, M., Snodgrass, C., de León, J., Licandro, J., Popescu, M., et al., 2022. Photometric observations of the binary near-earth asteroid (65803) didymos in 2015–2021 prior to dart impact. *The Planetary Science Journal* 3, 175. doi:<https://doi.org/10.3847/PSJ/ac7be1>.
- Quillen, A.C., LaBarca, A., Chen, Y., 2022. Non-principal axis rotation in binary asteroid systems and how it weakens the byorp effect. *Icarus* 374, 114826. doi:<https://doi.org/10.1016/j.icarus.2021.114826>.
- Quillen, A.C., Lane, M., Nakajima, M., Wright, E., 2020. Excitation of tumbling in phobos and deimos. *Icarus* 340, 113641. doi:<https://doi.org/10.1016/j.icarus.2020.113641>.
- Raducan, S.D., Jutzi, M., 2022. Global-scale reshaping and resurfacing of asteroids by small-scale impacts, with applications to the dart and hera missions. *The Planetary Science Journal* 3, 128. doi:<https://doi.org/10.3847/PSJ/ac67a7>.
- Richardson, D.C., Agrusa, H.F., Barbee, B., Bottke, W.F., Cheng, A.F., Eggl, S., Ferrari, F., Hirabayashi, M., Karatekin, Ö., McMahon, J., et al., 2022. Predictions for the dynamical states of the didymos system before and after the planned dart impact. *The Planetary Science Journal* 3, 157. doi:<https://doi.org/10.3847/PSJ/ac76c9>.
- Rivkin, A.S., Chabot, N.L., Stickle, A.M., Thomas, C.A., Richardson, D.C., Barnouin, O., Fahnestock, E.G., Ernst, C.M., Cheng, A.F., Chesley, S., et al., 2021. The double asteroid redirection test (dart): planetary defense investigations and requirements. *The Planetary Science Journal* 2, 173. doi:<https://doi.org/10.3847/PSJ/ac063e>.
- Scheeres, D.J., 2006. Relative equilibria for general gravity fields in the sphere-restricted full 2-body problem. *Celestial Mechanics and Dynamical Astronomy* 94, 317–349. doi:<https://doi.org/10.1007/s10569-005-6182-2>.
- Scheeres, D.J., 2009. Stability of the planar full 2-body problem. *Celestial Mechanics and Dynamical Astronomy* 104, 103–128. doi:<https://doi.org/10.1007/s10569-009-9184-7>.
- Scheirich, P., Pravec, P., 2009. Modeling of lightcurves of binary asteroids. *Icarus* 200, 531–547. doi:<https://doi.org/10.1016/j.icarus.2008.12.001>.
- Scheirich, P., Pravec, P., 2022. Preimpact mutual orbit of the dart target binary asteroid (65803) didymos derived from observations of mutual events in 2003–2021. *The Planetary Science Journal* 3, 163. doi:<https://doi.org/10.3847/PSJ/ac7233>.
- Scheirich, P., Pravec, P., Jacobson, S., Ďurech, J., Kušnirák, P., Hornoch, K., Mottola, S., Mommert, M., Hellmich, S., Pray, D., et al., 2015. The binary near-earth asteroid (175706) 1996 fg3—an observational constraint on its orbital evolution. *Icarus* 245, 56–63. doi:<https://doi.org/10.1016/j.icarus.2014.09.023>.
- Scheirich, P., Pravec, P., Kušnirák, P., Hornoch, K., McMahon, J., Scheeres, D., Čapek, D., Pray, D., Kučáková, H., Galád, A., et al., 2021. A satellite orbit drift in binary near-earth asteroids (66391) 1999 kw4 and (88710) 2001 sl9—indication of the byorp effect. *Icarus* 360, 114321. doi:<https://doi.org/10.1016/j.icarus.2021.114321>.
- Steinberg, E., et al., 2011. Binary yorp effect and evolution of binary asteroids. *The Astronomical Journal* 141, 55. doi:<https://doi.org/10.1088/0004-6256/141/2/55>.
- Stickle, A.M., DeCoster, M.E., Burger, C., Caldwell, W.K., Graninger, D., Kumamoto, K.M., Luther, R., Ormó, J., Raducan, S., Rainey, E., et al., 2022. Effects of impact and target parameters on the results of a kinetic impactor: predictions for the double asteroid redirection test (dart) mission. arXiv preprint arXiv:2209.06659.
- Taylor, P.A., Margot, J.L., 2010. Tidal evolution of close binary asteroid systems. *Celestial Mechanics and Dynamical Astronomy* 108, 315–338. doi:<https://doi.org/10.1007/s10569-010-9308-0>.
- Taylor, P.A., Margot, J.L., 2011. Binary asteroid systems: Tidal end states and estimates of material properties. *Icarus* 212, 661–676. doi:<https://doi.org/10.1016/j.icarus.2011.01.030>.
- Tiscareno, M.S., Thomas, P.C., Burns, J.A., 2009. The rotation of janus and epimetheus. *Icarus* 204, 254–261. doi:<https://doi.org/10.1016/j.icarus.2009.06.023>.
- Walsh, K.J., 2018. Rubble pile asteroids. *Annual Review of Astronomy and Astrophysics* 56, 593–624. doi:<https://doi.org/10.1146/annurev-astro-081817-052013>.
- Walsh, K.J., Richardson, D.C., Michel, P., 2008. Rotational breakup as the origin of small binary asteroids. *Nature* 454, 188–191. doi:<https://doi.org/10.1038/nature07078>.
- Wisdom, J., Peale, S.J., Mignard, F., 1984. The chaotic rotation of hyperion. *Icarus* 58, 137–152. doi:[https://doi.org/10.1016/0019-1035\(84](https://doi.org/10.1016/0019-1035(84)

